

Urban Heat Islands during Heat Waves: A Comparative Study between Boston and Phoenix

LIANG WANG^a AND DAN LI^a

^a *Department of Earth and Environment, Boston University, Massachusetts*

(Manuscript received 4 June 2020, in final form 24 February 2021)

ABSTRACT: In this study, we simulate the magnitude of urban heat islands (UHIs) during heat wave (HWs) in two cities with contrasting climates (Boston, Massachusetts, and Phoenix, Arizona) using the Weather Research and Forecasting (WRF) Model and quantify their drivers with a newly developed attribution method. During the daytime, a surface UHI (SUHI) is found in Boston, which is mainly caused by the higher urban surface resistance that reduces the latent heat flux and the higher urban aerodynamic resistance r_a that inhibits convective heat transfer between the urban surface and the lower atmosphere. In contrast, a daytime surface urban cool island is found in Phoenix, which is mainly due to the lower urban r_a that facilitates convective heat transfer. In terms of near-surface air UHI (AUHI), there is almost no daytime AUHI in either city. At night, an SUHI and an AUHI are identified in Boston that are due to the stronger release of heat storage in urban areas. In comparison, the lower urban r_a in Phoenix enhances convective heat transfer from the atmosphere to the urban surface at night, leading to a positive SUHI but no AUHI. Our study highlights that the magnitude of UHIs or urban cool islands is strongly controlled by urban–rural differences in terms of aerodynamic features, vegetation and moisture conditions, and heat storage, which show contrasting characteristics in different regions.

KEYWORDS: Extreme events; Atmosphere–land interaction; Surface fluxes; Numerical weather prediction/forecasting; Urban meteorology

1. Introduction

Despite having no universal definitions, heat waves (HWs) usually refer to a sustained period (typically more than 2 days) when the temperatures (e.g., daily maximum, mean, or minimum temperatures) exceed a certain threshold (Robinson 2001). Recent years have witnessed numerous disastrous HWs worldwide, such as the 2003 HW in Europe (García-Herrera et al. 2010), the 2010 Russian HW (Dole et al. 2011), and the 2013 HW in eastern China (Xia et al. 2016), incurring substantial socioeconomic costs (Xia et al. 2018) and raising concerns about human health (Campbell et al. 2018; Mora et al. 2017; Petkova et al. 2014), wildfires (Parente et al. 2018), crop failures (Fontana et al. 2015; Wreford and Adger 2010; Zampieri et al. 2017), and infrastructure damage (Rübelke and Vögele 2011). What is worse is that the intensity, duration, and frequency of HWs have been increasing and will likely continue to increase in many parts of the world in a warming climate (Brown et al. 2008; Donat et al. 2013; Fischer and Schär 2010; Lau and Nath 2012, 2014; Meehl and Tebaldi 2004; Schär et al. 2004; Tebaldi et al. 2006).

With the high thermal risks imposed by HWs in mind (Patz et al. 2005; Tan et al. 2010), the urban population, which comprises more than half of the world's population and is projected to reach 68% by 2050 (Grimm et al. 2008; United Nations 2019), usually experiences hotter conditions than the rural counterpart due to the well-known urban heat island (UHI) effects (Arnfield 2003; Oke 1982). The UHI effects have important impacts on the atmospheric boundary layer flow, the dispersion of pollutants, the energy and water consumption in cities, and so on (Han et al. 2014; Hidalgo et al. 2010; Miao et al.

2009; Pal et al. 2012; Zhang et al. 2014). The UHI intensity, which characterizes the magnitude of the UHI effect, is typically defined as the temperature difference between the urban and the surrounding rural areas, which can be based on either near-surface air temperature [i.e., air UHI (AUHI)] or surface temperature [i.e., surface UHI (SUHI)] (Stewart 2011). The negative AUHI and SUHI are called air urban cool island (AUCI) and surface urban cool island (SUCI), respectively, in this study.

Broadly, UHIs can be explained by the surface energy balance equation. For an imaginary control volume with an arbitrary horizontal scale that extends from the ground to the roof level and has no net horizontal advection of heat through the sides of the control volume, the energy balance equation can be expressed as (Oke et al. 2017)

$$AF + (1 - \alpha)SW_{in} + \varepsilon LW_{in} = H + LE + G + \varepsilon\sigma T_s^4, \quad (1)$$

where AF is the anthropogenic heat flux (W m^{-2}), α is the surface albedo, SW_{in} is the incoming shortwave radiation (W m^{-2}), ε is the surface emissivity, LW_{in} is the incoming longwave radiation (W m^{-2}), H is the sensible heat flux (W m^{-2}), LE is the latent heat flux (W m^{-2}), G is the ground heat flux (also called heat storage; W m^{-2}), σ is the Stefan–Boltzmann constant ($\text{W m}^{-2} \text{K}^{-4}$), and T_s is the land surface temperature (K). The terms on the left-hand side of Eq. (1) represent the energy input to the control volume either from anthropogenic emissions or from the radiation (after subtracting the reflected radiation), which includes the insolation and the longwave radiation from the atmosphere. The input energy can be transferred away from the control volume by either convection into the lower atmosphere (H), conduction into the ground (G), or radiation in the longwave band ($\varepsilon\sigma T_s^4$). Part of the input energy is consumed by the evapotranspiration process in order

Corresponding author: Dan Li, lidan@bu.edu

DOI: 10.1175/JAMC-D-20-0132.1

© 2021 American Meteorological Society. For information regarding reuse of this content and general copyright information, consult the AMS Copyright Policy (www.ametsoc.org/PUBSReuseLicenses).

to transform the water from the liquid phase to the vapor phase, namely, LE. UHIs are mainly caused by the unique urban characteristics such as less evapotranspiration associated with limited green space and low surface moisture, lower albedo owing to radiative trapping, and larger heat release at night due to the higher thermal admittance of built materials as well as the larger anthropogenic emissions (Arnfield 2003; Grimm et al. 2008; Grimmond 2007; Oke 1982; Ramamurthy et al. 2014; Taha 1997; Zhao et al. 2014). These unique urban characteristics either increase the energy input on the left-hand side of Eq. (1) or inhibit the efficiency of heat transfer on the right-hand side of the equation, leading to hotter urban surfaces and near-surface conditions.

Although the causes of UHIs are generally well understood, it remains a challenge to quantify and compare the contribution of each individual process to the magnitude of UHIs, which strongly depends on the nature of the urban and rural environments, human activities, and meteorological conditions (Grimmond 2007). Moreover, the spatial variations of UHIs across cities and background climates and their key controlling factors are still under debate (D. Li et al. 2019; Manoli et al. 2019; Zhao et al. 2014). To fill this research gap, the present study simulates the magnitude of UHIs during about 20 HW events in the period of 2007–16 over two cities in the United States (i.e., Boston, Massachusetts, and Phoenix, Arizona) with the Weather Research and Forecasting (WRF) Model. The objective of this study is to quantify and compare the underlying drivers of UHIs during HWs in these two cities with contrasting background climates. Specifically, Boston has a humid continental climate while Phoenix has a hot desert climate. The annual mean temperature is 9.8°C in Boston and 21.5°C in Phoenix, and the annual mean rainfall is 1122 mm in Boston, while it is only 211 mm in Phoenix. Therefore, conducting the same analyses over these two cities can provide insights into the spatial variability of UHIs and their controlling factors.

The paper is organized as follows: section 2 describes the data and method, section 3 presents the main results, section 4 discusses the implications and limitations of our work, and section 5 concludes the paper.

2. Data and method

a. Observational data

To identify HWs, we use the 2-m air temperatures from the Integrated Surface Database (ISD) provided by the National Oceanic and Atmospheric Administration (NOAA; ncdc.noaa.gov/isd/data-access) and measured at the Boston Logan International Airport and the Phoenix Sky Harbor International Airport. These data are used because of their long-term span, which is required for HW identification. However, for validation of WRF simulation results, we use the 2-m air temperatures from the Meteorological Assimilation Data Ingest System (MADIS; madis-data.ncep.noaa.gov/madisPublic1/data/archive) due to their larger spatial coverage (see blue triangles on Figs. 1a and 1c). We only use the MADIS stations whose data availability in the simulation period is more than 90%.

To evaluate the WRF-simulated boundary layer structure, we use commercial aircraft data provided by the Aircraft Communications Addressing and Reporting System (ACARS; madis-data.cprk.ncep.noaa.gov/madisPublic1/data/archive). The ACARS data are proved to be as good as the radiosonde data in terms of quality in the lower atmosphere, but with much higher temporal and vertical resolutions (Petersen 2016; Zhang et al. 2019). Specifically, the root-mean-square error (RMSE) of ACARS against radiosonde below 850 hPa is approximately 1.3 K, while the mean bias error (MBE) falls between -0.16 and -0.32 K (Zhang et al. 2019). In this study, we use the temperature profiles collected by aircraft when they take off or land at Boston Logan International Airport and Phoenix Sky Harbor International Airport (see blue circles on Figs. 1b and 1d) that have been processed and interpolated onto regular height levels at the hourly scale (Zhang et al. 2019, 2020).

To validate the WRF-simulated land surface temperatures, we use the land surface temperature data from the 1-km MOD11A1, version 6, product provided by the Moderate Resolution Imaging Spectroradiometer (MODIS; lpdaac.usgs.gov/products/mod11a1v006).

b. HW identification

The HW definitions used in previous studies vary in terms of the temperature variable, the threshold of its magnitude, and the duration/extent (Anderson and Bell 2011; Chen and Zhai 2017; Lau and Nath 2014; Liao et al. 2018a; Luo and Lau 2017; Meehl and Tebaldi 2004; Peng et al. 2011; Perkins 2015; Sillmann et al. 2013; Yang et al. 2017). In our research, we identify a HW as a period of at least two consecutive days whose daily mean temperature exceeds the 95 percentile of the local climatology (Anderson and Bell 2009, 2011; Hajat et al. 2006; Zhang et al. 2020), which is defined based on daily mean temperatures during the warm seasons (from 1 May to 30 September) of 2007–16. The thresholds of two days and 95 percentile are used to ensure enough HW days selected for our analysis and also distinct thermal conditions between HW and non-HW days. We further corroborate these selected HWs using the ACARS temperature profiles (i.e., we manually check if the start and the end of selected HWs coincide with obvious changes in the ACARS temperature profiles; see Zhang et al. 2020). Overall, 41 HWs are selected during 2007–16, with 20 HWs in Boston and 21 HWs in Phoenix (Table 1).

c. WRF simulations

The WRF Model has been widely used to study urban climate (Chen et al. 2011; Georgescu et al. 2011; Heaviside et al. 2015; Li and Bou-Zeid 2014; H. Li et al. 2019; Meir et al. 2013; Ramamurthy et al. 2017; Ramamurthy and Bou-Zeid 2016; Tewari et al. 2019). In this study, the WRF, version 4.0, is used to simulate each HW event, with 5 pre-HW days and 5 post-HW days. Three nested model domains with spatial resolutions of 9, 3, and 1 km, respectively, are used (Fig. 1). For Boston, these three domains have 149×149 , 150×150 , and 150×150 grid cells, respectively. The 9-km domain covers most of the northeastern United States, and the innermost domain covers

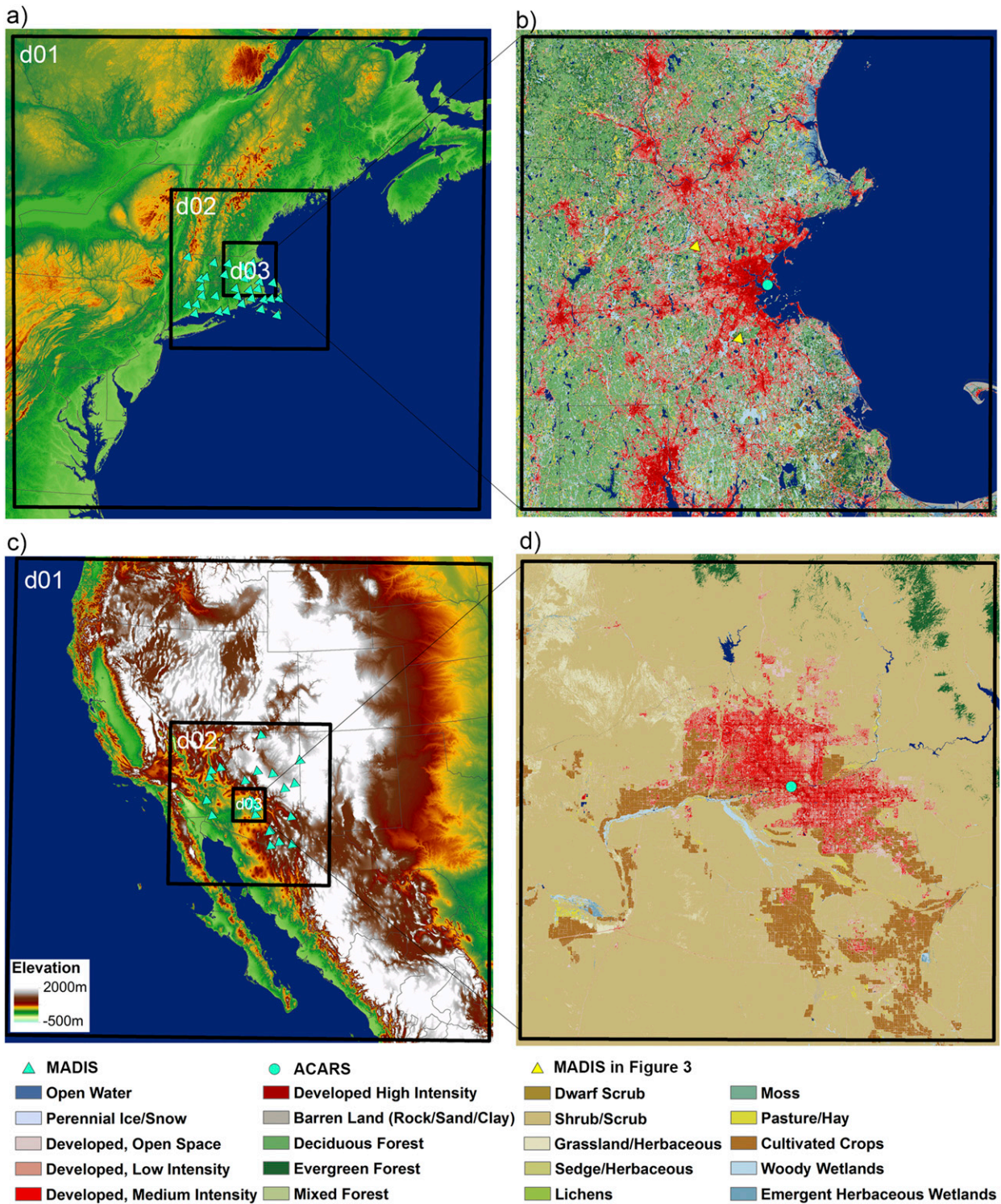


FIG. 1. The (left) WRF domain configuration and terrain height and (right) land-use map over (a),(b) Boston and (c),(d) Phoenix. In (b), the yellow triangles mark the locations of the two MADIS sites used in Fig. 3, below. The northern one is an urban site KBED at 42.47°N, 71.28°W, and the southern one is a rural site KMQE at 42.21°N, 71.11°W. The blue circles mark the locations of the Boston and Phoenix airports.

TABLE 1. Identified heat waves (HW) during 2007–16 in Boston and Phoenix. The asterisk indicates that the HW is selected for validation.

Boston			Phoenix		
Case No.	Date	HW days	Case No.	Date	HW days
1*	25–28 Jun 2007	4	21*	5–6 Jul 2007	2
2	2–4 Aug 2007	3	22	17–19 Jul 2007	3
3	17–19 Aug 2009	3	23	12–13 Aug 2007	2
4	3–6 Jul 2010	4	24	16–17 Jun 2008	2
5	16–18 Jul 2010	3	25	10–14 Jul 2009	5
6	28–29 Jul 2010	2	26	16–19 Jul 2009	4
7*	29 Aug–2 Sep 2010	5	27	27–28 Jul 2009	2
8	17–18 Jul 2011	2	28	3–6 Aug 2009	4
9	21–23 Jul 2011	3	29	14–16 Jul 2010	3
10	20–22 Jun 2012	3	30*	1–3 Jul 2011	3
11	29 Jun–1 Jul 2012	3	31	23–26 Aug 2011	4
12	15 Jul–17 Jul 2012	3	32	29 Aug–1 Sep 2011	4
13	30 May–2 Jun 2013	4	33	7–11 Jul 2012	5
14	23–25 Jun 2013	3	34	6–14 Aug 2012	9
15	3–7 Jul 2013	5	35	28–30 Jun 2013	3
16*	14–20 Jul 2013	7	36	16–17 Aug 2013	2
17	12–16 Jul 2016	5	37	22–24 Jul 2014	3
18	21–23 Jul 2016	3	38	17–19 Jun 2015	3
19	11–12 Aug 2016	2	39	14–16 Aug 2015	3
20	14–15 Aug 2016	2	40*	19–20 Jun 2016	2
			41	26–28 Jul 2016	3

Boston as well as the surrounding landscapes, which are mostly forests. For Phoenix, these three domains have 299×299 , 300×300 , and 180×180 grid cells, respectively. The 9-km domain covers most of the southwestern United States as well as a sizeable portion of Mexico, and the innermost domain covers Phoenix and the surrounding landscapes, which are mostly scrublands. All model domains have 55 vertical levels, and the model top is set as 100 hPa. The North American Regional Reanalysis (NARR) data with a spatial resolution of about 32 km and a temporal resolution of 3 h are used for the initial and boundary conditions. National Land Cover Database 2011 (NLCD 2011) is used as land-use input to the model (Homer et al. 2015). When used in WRF, this land-cover dataset has a spatial resolution of 9 arc s. The urban land is classified into three categories (commercial urban, high-intensity residential urban, and low-intensity residential urban). Thus, not all urban grid cells have the same surface properties. The physical parameterizations for the WRF simulations follow closely the studies by Li and Bou-Zeid (2014) and Wang and Li (2019), including the Dudhia scheme for shortwave radiation (Dudhia 1989), the Rapid Radiative Transfer Model (RRTM) scheme for longwave radiation (Mlawer et al. 1997), the single-moment 6-class microphysics scheme (WSM6; Hong and Lim 2006), and the Noah land surface model (Ek et al. 2003) coupled with the single-layer urban canopy model (Kusaka et al. 2001; Kusaka and Kimura 2004). Following Wang and Li (2019), we test three planetary boundary layer (PBL) schemes: the asymmetric convective model, version 2 (ACM2), scheme (Pleim 2007); the Yonsei University (YSU) scheme (Hong et al. 2006); and the Mellor–Yamada–Janjić (MYJ) scheme (Mellor and Yamada 1974). We focus on a sensitivity test to the PBL

scheme as turbulent heat transfer is an extremely important process that regulates the magnitude of UHIs (Li and Bou-Zeid 2014). For model validation, we select six HW events with more complete observational records (denoted with an asterisk in Table 1). We will use the validation results to select a PBL scheme with the best consistency with the observational data, which will be used for simulating the remaining HW events.

d. The attribution method

1) ATTRIBUTION OF SUHI

The attribution of SUHI is based on the Two-Resistance Mechanism (TRM) model used in a number of recent studies (Chen et al. 2020; D. Li et al. 2019; Li and Wang 2019; Liao et al. 2018b; Moon et al. 2020; Rigden and Li 2017; Wang et al. 2019, 2020). The TRM model starts from the surface energy balance equation as Eq. (1), with H and LE parameterized using the concepts of aerodynamic resistance and surface resistance (Brutsaert 1982, 2005; Monteith and Unsworth 2007), as follows:

$$H = \frac{\rho c_p}{r_a} (T_s - T_a) \quad \text{and} \quad (2)$$

$$\text{LE} = \frac{\rho L_v}{r_a + r_s} [q^*(T_s) - q_a], \quad (3)$$

where ρ is the air density (kg m^{-3}), c_p is the specific heat of air at constant pressure ($\text{J kg}^{-1} \text{K}^{-1}$), r_a is the aerodynamic resistance between the surface and the lower atmosphere (s m^{-1}), T_a is the potential temperature of the lower atmosphere (K; not the near-surface or 2-m air temperature as discussed below), L_v is the latent heat

of vaporization (J kg^{-1}), r_s is the surface resistance (s m^{-1}), q^* is the saturated specific humidity at T_s (kg kg^{-1}), and q_a is the specific humidity of the lower atmosphere (kg kg^{-1}). The aerodynamic resistance r_a represents the efficiency with which the land surface convects sensible heat to the lower atmosphere (Brutsaert 1982, 2005; Garratt 1992). It is controlled mostly by the capacity of atmospheric turbulence in transporting sensible heat but also molecular diffusion at the interface between the land and the atmosphere (Brutsaert 1982, 2005; Garratt 1992). From Eq. (2) one can see that a higher aerodynamic resistance results in a lower sensible heat flux with a given temperature gradient. On the other hand, the surface resistance r_s represents the efficiency with which water is extracted from

the saturated zone to the surface or from the vegetation inside to the leaf surface, which is strongly dependent on soil moisture and vegetation stresses (Brutsaert 1982, 2005; Garratt 1992). From Eq. (3) one can see that moisture transfer from the land to the atmosphere also experiences the r_a , in addition to r_s . With everything else being equal, a higher surface resistance leads to a smaller latent heat flux.

Substituting Eqs. (2) and (3) into Eq. (1) yields a nonlinear equation for T_s , which is further linearized by applying first-order Taylor series expansion to the outgoing longwave radiation and the saturated specific humidity terms, so that an analytical expression for T_s can be obtained:

$$T_s = \frac{\text{AF} + \text{SW}_{\text{in}}(1 - \alpha) + \varepsilon \text{LW}_{\text{in}} - \varepsilon \sigma T_a^4 - G - \frac{\rho L_v}{r_a + r_s} [q^*(T_s) - q_a]}{4\varepsilon \sigma T_a^3 + \frac{\rho c_p}{r_a} + \frac{\rho L_v}{(r_a + r_s)} \frac{\partial q^*}{\partial T} \Big|_{T_a}} + T_a. \quad (4)$$

Based on this solution, the difference in the surface temperature between urban and rural surfaces can be further expressed

as the sum of the contributions from various factors again using first-order Taylor series expansion, as follows:

$$\begin{aligned} \Delta T_s = & \left(\frac{\partial T_s}{\partial \text{AF}} \right) \Delta \text{AF} + \left(\frac{\partial T_s}{\partial \varepsilon} \right) \Delta \varepsilon + \left(\frac{\partial T_s}{\partial \alpha} \right) \Delta \alpha + \left(\frac{\partial T_s}{\partial G} \right) \Delta G + \left(\frac{\partial T_s}{\partial r_a} \right) \Delta r_a + \left(\frac{\partial T_s}{\partial r_s} \right) \Delta r_s + \left(\frac{\partial T_s}{\partial \text{SW}_{\text{in}}} \right) \Delta \text{SW}_{\text{in}} \\ & + \left(\frac{\partial T_s}{\partial \text{LW}_{\text{in}}} \right) \Delta \text{LW}_{\text{in}} + \left(\frac{\partial T_s}{\partial T_a} \right) \Delta T_a + \left(\frac{\partial T_s}{\partial q_a} \right) \Delta q_a + \left(\frac{\partial T_s}{\partial P} \right) \Delta P, \end{aligned} \quad (5)$$

where P is the pressure (Pa) and Δ indicates the urban–rural difference in each factor (i.e., urban minus rural values). In Eq. (5), the partial derivative represents the sensitivity of the surface temperature to a change in each factor, whose analytical formulation can be obtained using Eq. (4). Throughout the paper, each term on the right-hand side of Eq. (5) will be called a contribution. Each contribution is the product of the sensitivity (Table 3), which represents how sensitive the surface temperature is to a change in each factor, and the difference (Table 5), which represents the urban–rural contrast of that factor (i.e., urban minus rural values).

Compared with previous attribution methods [such as D. Li et al. (2019) and Zhao et al. (2014)], Eq. (5) not only considers the influence of differences in land surface biophysical parameters (such as albedo) on SUHIs, but also the influence of differences in atmospheric conditions (such as incoming shortwave radiation) on SUHIs. This is important for our study because, unlike previous studies assuming that urban and rural lands share the same atmospheric conditions due to their use of subgrid outputs from global climate or Earth system models (D. Li et al. 2019; Zhao et al. 2014), the SUHIs in our study are the surface temperature differences between urban and rural grid cells, which have different overlying atmospheric conditions.

2) ATTRIBUTION OF AUHI

The original TRM method was designed for the attribution of surface temperature differences (i.e., SUHIs). In this study, we further develop the TRM method to attribute the near-surface air temperature differences (i.e., AUHIs). The mathematical link between the surface temperature and near-surface air temperature is provided by the constant heat flux assumption in the atmospheric surface layer. This assumption is the basis for deriving the so-called 2-m air temperature in models like WRF. With this assumption, the sensible heat flux derived from the temperature difference between the land surface and the lower atmosphere [i.e., Eq. (2)] should be equal to the sensible heat flux derived from the temperature difference between the air at 2 m above the displacement height and the lower atmosphere. Thus the 2-m air temperature T_2 can be related to the surface temperature T_s and the potential temperature of the lower atmosphere T_a , as follows:

$$T_2 = \frac{r'_a}{r_a} (T_s - T_a) + T_a, \quad (6)$$

where r'_a is the aerodynamic resistance between the reference height (i.e., 2 m above the displacement height) and the lower atmosphere (s m^{-1}). Hence, r'_a is different from r_a , which is the aerodynamic resistance between the surface and the lower atmosphere.

Thus, the urban–rural difference in the 2-m air temperature can be expressed as follows:

$$\Delta T_2 = f \left(\frac{\partial T_s}{\partial \text{AF}} \right) \Delta \text{AF} + f \left(\frac{\partial T_s}{\partial \varepsilon} \right) \Delta \varepsilon + f \left(\frac{\partial T_s}{\partial \alpha} \right) \Delta \alpha + f \left(\frac{\partial T_s}{\partial G} \right) \Delta G + \left[f \left(\frac{\partial T_s}{\partial r_a} \right) - \frac{r'_a}{r_a^2} (T_s - T_a) \right] \Delta r_a + \left(\frac{T_s - T_a}{r_a} \right) \Delta r'_a + f \left(\frac{\partial T_s}{\partial r_s} \right) \Delta r_s + f \left(\frac{\partial T_s}{\partial \text{SW}_{\text{in}}} \right) \Delta \text{SW}_{\text{in}} + f \left(\frac{\partial T_s}{\partial \text{LW}_{\text{in}}} \right) \Delta \text{LW}_{\text{in}} + \left[f \left(\frac{\partial T_s}{\partial T_a} \right) - f + 1 \right] \Delta T_a + f \left(\frac{\partial T_s}{\partial q_a} \right) \Delta q_a + f \left(\frac{\partial T_s}{\partial P} \right) \Delta P, \quad (7)$$

where $f = r'_a/r_a$. Again, Δ indicates the urban–rural difference in each factor (Table 5) while the remainder of each term represents the sensitivity of T_2 to each factor (Table 4).

e. Application of the attribution method to the WRF outputs

The attribution analysis in general follows previous research by Liao et al. (2018b) and D. Li et al. (2019). Most variables needed in Eqs. (5) and (7) are direct outputs of the WRF Model including the surface temperature, 2-m air temperature, emissivity, albedo, ground heat flux, incoming shortwave radiation, incoming longwave radiation, pressure, and the potential temperature at the lowest level of the atmospheric model (which is about 30 m in our simulations). The specific humidity is calculated from the water vapor mixing ratio (QVAPOR) through $q_a = \text{QVAPOR}/(\text{QVAPOR} + 1)$. Since our WRF simulations do not include anthropogenic heat fluxes in the form of both sensible and latent heat, AF is set to zero in the attribution. The implication of neglecting anthropogenic heat fluxes will be discussed in section 4b.

The aerodynamic resistances (r_a and r'_a) and the surface resistance r_s are not direct outputs from the WRF Model. To infer them at the gridcell scale, we use the WRF simulated sensible and latent heat fluxes, as well as the surface temperature, 2-m air temperature, and the potential temperature and specific humidity at the lowest level of the atmospheric model following Eqs. (2), (3), and (6). It should be stressed that we use the potential temperature and specific humidity at the lowest level of the atmospheric model (~ 30 m), instead of the 2-m air temperature and specific humidity, to represent T_a and q_a in Eqs. (2), (3), and (6), because the 2-m air temperature and specific humidity are not prognostic variables in the model. We also stress that r_a is different from r'_a , arising from the fundamental dependence of aerodynamic resistance on the height z in the bulk formulations for surface fluxes (Garratt 1992): r_a represents the resistance to convective heat transfer between the surface and the lowest level of the atmospheric model while r'_a represents the resistance to convective heat transfer between the reference height (i.e., 2 m above the displacement height) and the lowest level of the atmospheric model.

The aerodynamic resistances and surface resistance are inferred using Eqs. (2), (3), and (6) at the hourly scale for grid cells in the innermost domain. In this study, we only consider grid cells with the dominant urban land cover (i.e., high-intensity residential urban for both cities) and the dominant rural land cover (i.e., evergreen forest for Boston and shrub for Phoenix). In total, there are 1372 urban grid cells and 1798 rural grid cells in Boston and 1452 urban grid cells and 25 502 rural grid cells in Phoenix. We consider only one urban type because each urban type corresponds to a unique set of urban parameters and thus considering only one urban type simplifies

the comparison between the two cities and reveals more information about the role played by the background climate. We use the default values of urban parameters in WRF (Chen et al. 2011). The high-intensity residential urban corresponds to the average building height of 7.5 m, the average roof and road widths of 9.4 m, and the impervious surface fraction of 0.9. Other thermodynamic parameters such as albedo, emissivity, heat capacity, and thermal conductivity can be found in Chen et al. (2011). When the resistances are estimated at the hourly scale, they may be of negative values, especially for aerodynamic resistances. This issue is fundamentally linked to the fact that the TRM model parameterizes turbulent heat fluxes using the bulk transfer relations [i.e., Eqs. (2) and (3)], which are local turbulence closures and assume uniform distributions of heat sources at the surface (i.e., with a single surface temperature). In the WRF Model, the heat sources are not uniformly distributed (e.g., the single-layer urban canopy model considers the roof, the wall, and the ground separately). In this situation, the inferred aerodynamic resistances [e.g., based on Eq. (2)] might appear to be negative. Since the negative resistances are physically meaningless, the grid cells with negative aerodynamic or surface resistances are filtered out following previous work (D. Li et al. 2019; Liao et al. 2018b). The numbers of the filtered urban/rural grid cells vary from hour to hour. For Boston, they are on average about 6% during the daytime and about 56% during the nighttime. For Phoenix, they are on average about 1% during the daytime and about 3% during the nighttime. To further reduce the uncertainties of the inferred resistances, we remove the grid cells in which the magnitudes or absolute values of sensible and latent heat fluxes are smaller than 15 W m^{-2} in the daytime (1000–1600, local standard time) and 0.1 W m^{-2} in the nighttime (2200–0400, local standard time). These thresholds are needed because the fluxes appear in the denominator when inferring the resistances. The exact values of these thresholds are chosen as a compromise between ensuring that the uncertainty of the inferred resistance is sufficiently small but simultaneously maintaining a reasonably large sample of grid cells. After applying these data-filtering strategies, there remain on average about 1300 and 350 urban grid cells in Boston during the daytime and nighttime, respectively, and 1500 and 1000 rural grid cells in Boston during the daytime and nighttime, respectively. For Phoenix, there are on average about 200 and 100 urban grid cells during the daytime and nighttime, respectively, and about 10 000 and 20 000 rural grid cells during the daytime and nighttime, respectively. We note that these data-filtering strategies are only applied when the attribution analysis is conducted (i.e., in section 3c). The consistency between the average diurnal cycle results in section 3b and the attribution results in section 3c, as shall

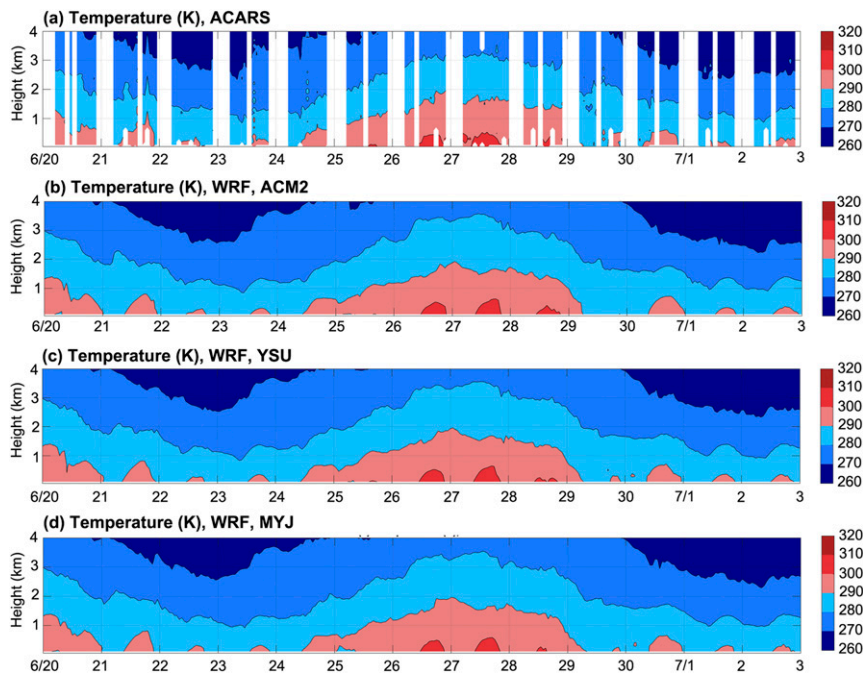


FIG. 2. The evolution of the air temperature profile in the lowest 4 km at Boston Logan International Airport from 20 Jun to 3 Jul 2007; 25–28 June is the heat-wave period. Shown are (a) ACARS data and WRF simulation results with the (b) ACM2, (c) YSU, and (d) MYJ schemes. The height is above ground level. The blank areas are due to the lack of ACARS data, which typically occurs from late night to early morning.

be seen later, implies that these data-filtering strategies do not alter our key findings.

Then we spatially average each variable across the dominant urban and rural land-cover types, which results in one urban value and one rural value for each variable in each hour. After performing the spatial average, we further average the data over daytime and nighttime for each HW day and then conduct the attribution analysis at the daytime average and nighttime average scales (hereinafter the daily scale). In doing so, the consistency between the TRM modeled UHIs and the WRF simulated UHIs is higher compared to performing the attribution at the hourly scale and then aggregating the results to the daily scale. This is similar to what previous studies found (D. Li et al. 2019; Liao et al. 2018b).

3. Results

a. Assessment of the WRF simulations with different PBL schemes

This section aims to assess the WRF-simulated results, with a focus on comparing the performances of WRF with different PBL schemes. To do so, 6 of the 41 HWs are selected (noted with an asterisk in Table 1), with 3 in Boston and 3 in Phoenix.

First, we validate the WRF-simulated temperature profiles against the ACARS observations at the airports. Figure 2 shows an example (HW case 1; 25–28 June 2007) in Boston. We find that the WRF Model simulates the “heat dome” over HW

days (25–28 June) as observed by the ACARS data. A significant warming and a sharp cooling are captured by WRF in the lowest 4 km of the atmosphere on the days right before (24 June) and after (29 June) the HW, respectively (Figs. 2b–d). We do not observe obvious differences among the WRF simulations with different PBL schemes (Figs. 2b–d), which is also reflected by the similar RMSEs between the WRF simulated results with the three PBL schemes and the ACARS data (Table 2). When the validation against the ACARS data is further applied to the other 5 HW cases, the weighted average RMSEs in Table 2 show that ACM2 is slightly superior to the other two PBL schemes but the differences between the PBL schemes are rather small.

Second, we validate the WRF-simulated 2-m air temperatures against the weather station data from MADIS. Figure 3 shows the results from the same HW event as in Fig. 2 at two weather stations (i.e., the urban site KBED and the rural site KMQE in Boston marked by yellow triangles in Fig. 1b). Although some biases exist, the WRF-simulated results show overall good agreement with the observations and can reasonably reflect the onset and demise of the HW. Different PBL schemes show contrasting performances. For example, at the urban site KBED (Figs. 3a,c,e), the WRF results using MYJ deviate from the observations more strongly than those using the other two PBL schemes. However, at the rural site KMQE (Figs. 3b,d,f), the WRF results with MYJ are closer to the observations than those with the other two PBL schemes. The weighted average RMSEs based upon all available weather

TABLE 2. Averaged RMSEs between the model simulated results and the observations (MADIS and ACARS) over six heat waves. Availability refers to the percentage of available data for the whole HW period, including 5 pre-HW days, all HW days, and 5 post-HW days. The weighted mean RMSE is calculated based upon the weight of the sample size.

Case No.	ACARS					MADIS				
	ACM2	YSU	MYJ	Availability (%)	Sample size	ACM2	YSU	MYJ	Availability (%)	Sample size
1	1.91	1.90	1.89	64.48	21946	2.16	2.13	2.50	99.06	10015
7	2.21	2.21	2.17	60.42	22031	2.04	2.05	2.44	96.91	10495
16	2.31	2.45	2.47	60.18	24861	2.35	2.27	2.43	98.79	10505
21	2.32	2.26	2.45	46.65	13618	3.05	3.19	3.60	98.93	6290
30	2.47	2.45	2.73	65.62	20743	3.11	3.09	3.34	98.49	6782
40	2.76	2.78	2.79	88.81	25922	2.91	3.03	3.49	99.87	4618
Weighted mean	2.33	2.34	2.42			2.49	2.50	2.82		

station data (Table 2) show that ACM2 is slightly better than YSU, with MYJ showing the worst performance, which is consistent with the previous findings using ACARS.

Third, we compare the land surface temperatures simulated by WRF and remotely sensed by MODIS. Figure 4 shows two snapshots of the simulated and observed land surface temperature patterns at around 1100 and 2100 (local standard

time) 27 June 2007 in Boston. Unlike ACARS and MADIS that have continuous observations over the course of the day, MODIS only provides land surface temperature measurements at its overpassing time. Moreover, the availability of MODIS data is often reduced by the presence of clouds. For this particular HW day, the WRF simulations are able to capture the broad urban–rural land surface temperature

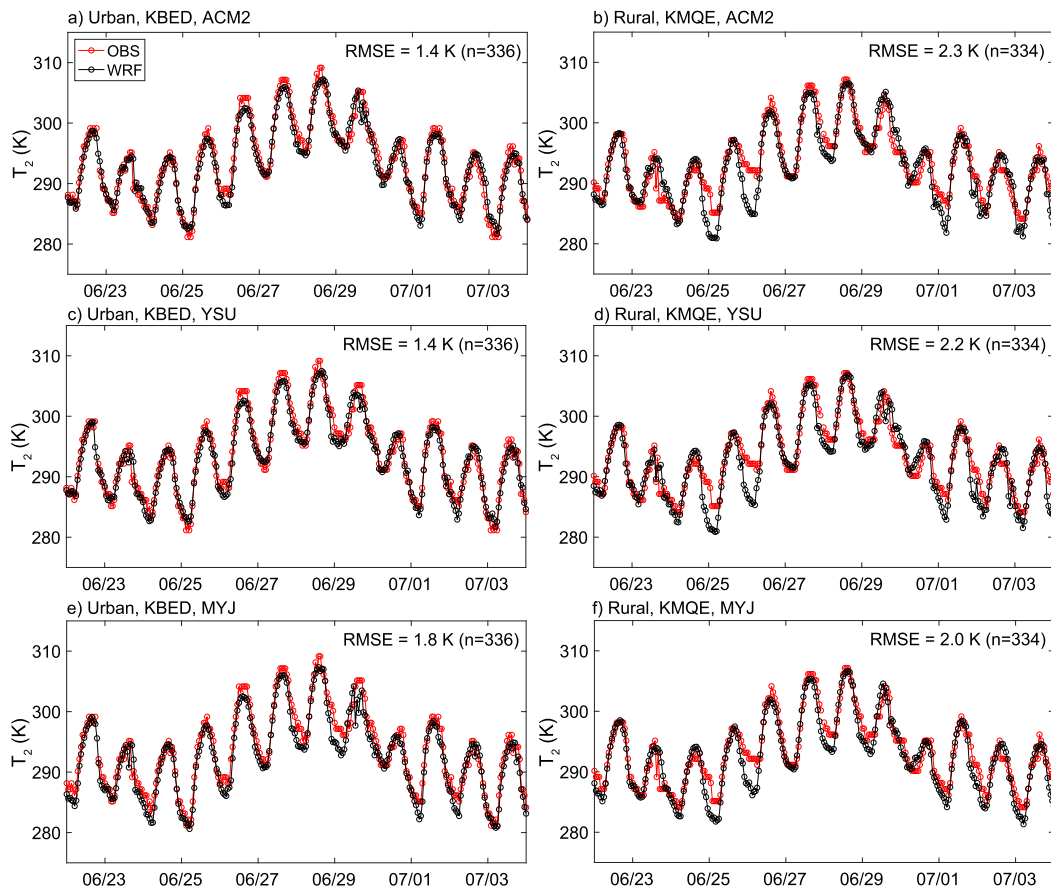


FIG. 3. Comparisons between WRF-simulated (black circles) and MADIS weather-station-measured (red circles) 2-m air temperature from 20 Jun to 3 Jul 2007 in Boston; 25–28 June is the heat-wave period. Shown are comparisons at (left) an urban site (KBED) and (right) a rural site (KMQE) for WRF simulations with (a),(b) ACM2; (c),(d) YSU; and (e),(f) MYJ. See the yellow triangles in Fig. 1 for the locations of KBED and KMQE. RMSE and sample size n are denoted in the upper-right corner of each panel.

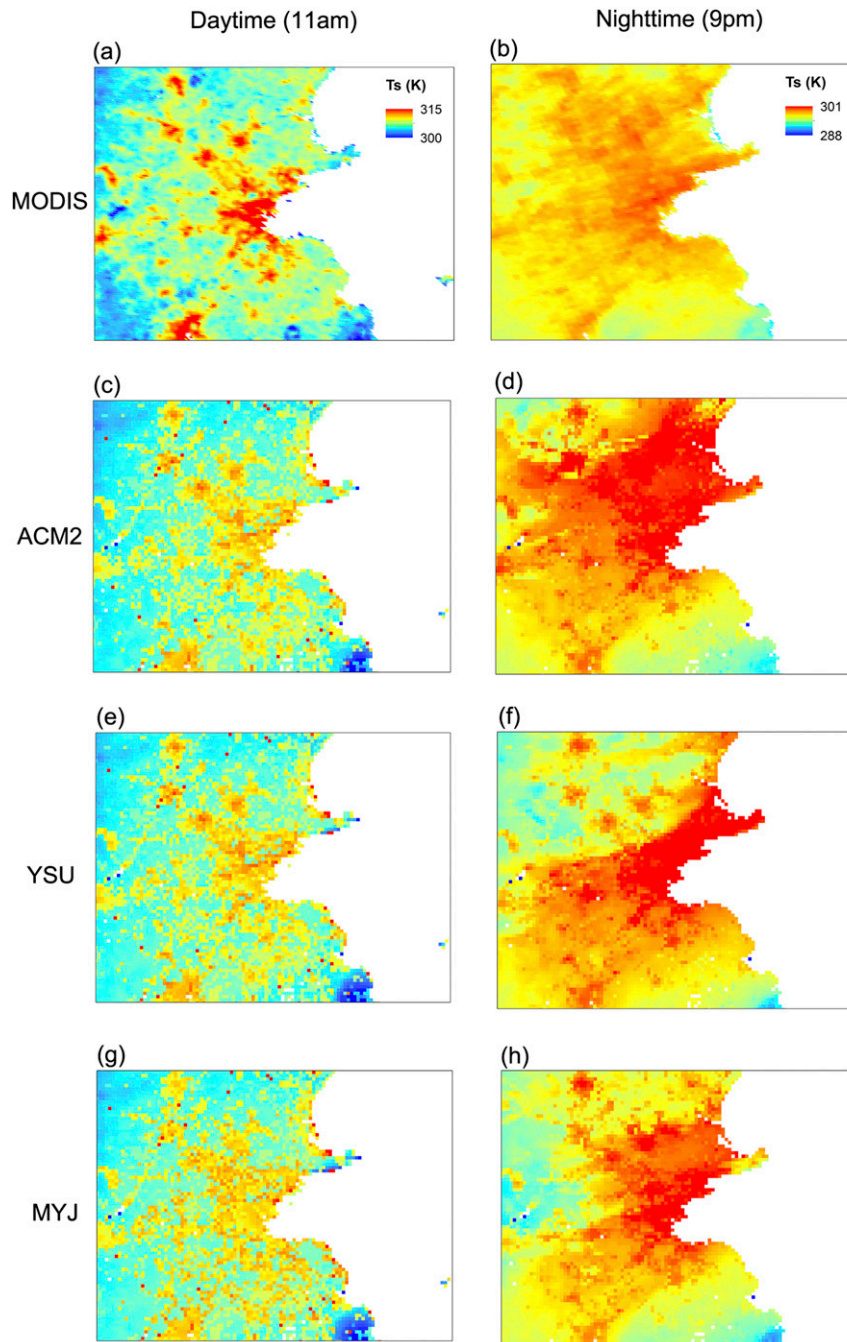


FIG. 4. Land surface temperatures from (a),(b) MODIS and WRF simulations using (c),(d) ACM2; (e),(f) YSU; and (g),(h) MYJ schemes at (left) 1100 and (right) 2100 local standard time 27 Jun 2007 in Boston.

contrast, with some underestimation of SUHI during the daytime and overestimation during the nighttime. When the temperatures are averaged over urban areas during the daytime (nighttime), the WRF simulations yield 311.0 K (300.5 K), 311.2 K (300.2 K), and 310.4 K (299.6 K) for ACM2, YSU, and MYJ, respectively; and the MODIS gives 312.3 K (298.4 K). For the rural average land surface temperatures during the daytime

(nighttime), the WRF simulations yield 304.7 K (296.2 K), 304.8 K (295.2 K), and 305.0 K (294.9 K) for ACM2, YSU, and MYJ, respectively, and the MODIS gives 305.7 K (296.3 K).

The performance of the WRF Model presented here is broadly consistent with previous studies (Kalverla et al. 2016; Li and Bou-Zeid 2014; Liao et al. 2014; Meir et al. 2013; Ramamurthy et al. 2017; Salamanca et al. 2018; Wang and Li 2019). Based on the

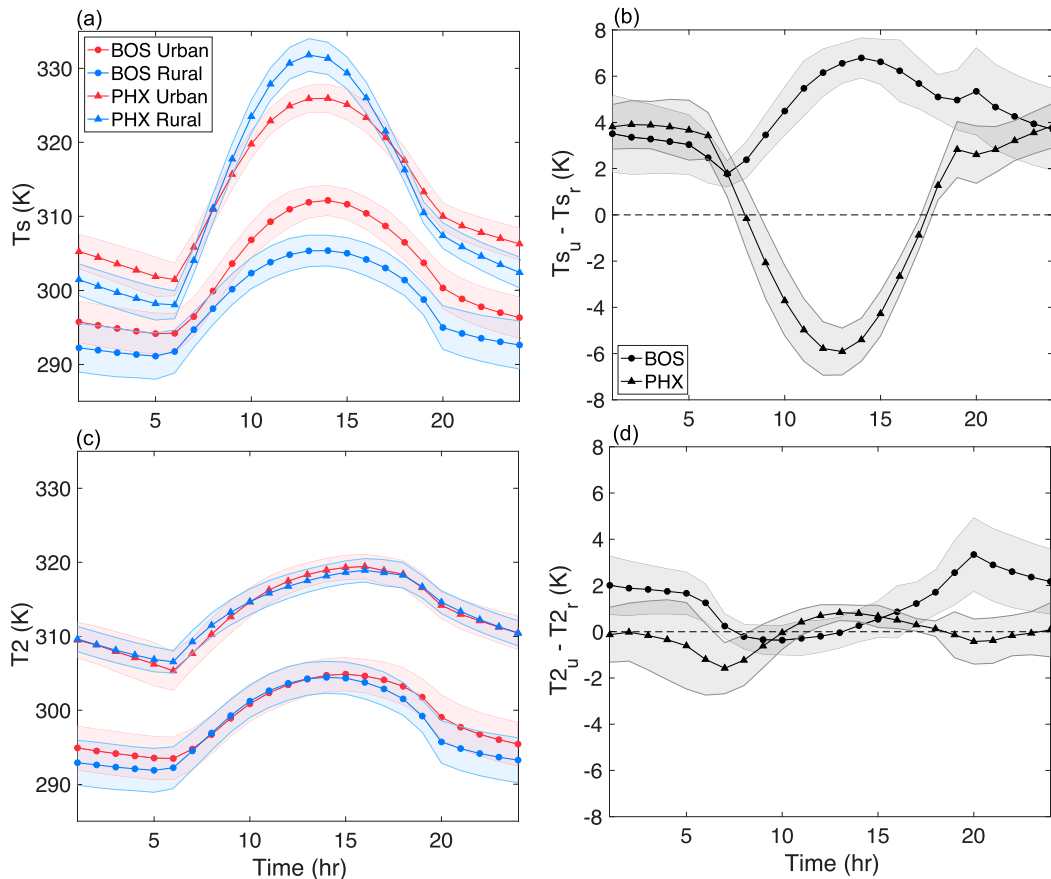


FIG. 5. Average diurnal cycles of (a) surface temperatures T_s and (c) 2-m air temperature T_2 and the urban-rural (urban minus rural temperature) differences in (b) surface temperature and (d) 2-m air temperature from WRF simulations. The shading denotes standard deviations. BOS = Boston; PHX = Phoenix. Time represents the local standard time.

findings from Figs. 2-4 and Table 2, we choose the ACM2 scheme to perform simulations for the remaining HW cases.

b. WRF-simulated urban-rural differences in temperatures and fluxes

In this section, we investigate the WRF-simulated urban-rural differences in surface and 2-m air temperatures and fluxes using average diurnal cycles over HW days. The average diurnal cycles present a general picture of urban-rural contrasts during HWs and how they differ between day and night and between Boston and Phoenix.

During the daytime (1000-1600, local standard time), Phoenix is much hotter than Boston (Figs. 5a,c), as expected from its lower latitude and desert climate. When the urban and rural surface temperatures are compared, Boston shows a daytime SUHI, while Phoenix presents a daytime SUCI (Fig. 5b). During the nighttime (2100-0400, local standard time), both cities show an SUHI (Fig. 5b). Compared to the surface temperature, the 2-m air temperature shows smaller differences between cities (Fig. 5c) and also smaller urban-rural differences for each city (Fig. 5d). As far as the daytime and nighttime average results are concerned, Phoenix shows almost no AUHI during both

daytime and nighttime; Boston shows no AUHI during the daytime but a nighttime AUHI (Fig. 5d). However, we also point out that there are some variations within the daytime/nighttime periods. For example, the urban-rural differences of 2-m air temperature in both cities drop in the early morning, which is possibly due to the rapid growth of the convective boundary layer as shown by Theeuwes et al. (2015).

The radiative fluxes including incoming shortwave and longwave radiation, and outgoing shortwave and longwave radiation are examined in Fig. 6. During the daytime, the incoming shortwave radiation of Phoenix is on average larger than that of Boston due to its lower latitude (Fig. 6a). Within each city, the incoming shortwave radiation is nearly identical for both urban and rural surfaces (Fig. 6a). Note that we did not modify the aerosol profiles in WRF, and thus the urban-rural difference in terms of aerosol loading is not considered here. In contrast, the urban-rural difference in outgoing shortwave radiation is large (Fig. 6c), which reflects the large urban-rural contrast of albedo considering that the urban-rural difference in incoming shortwave radiation is rather small. Specifically, the urban land of Boston has a higher surface albedo than the rural land of Boston (forests) and thus reflects more shortwave

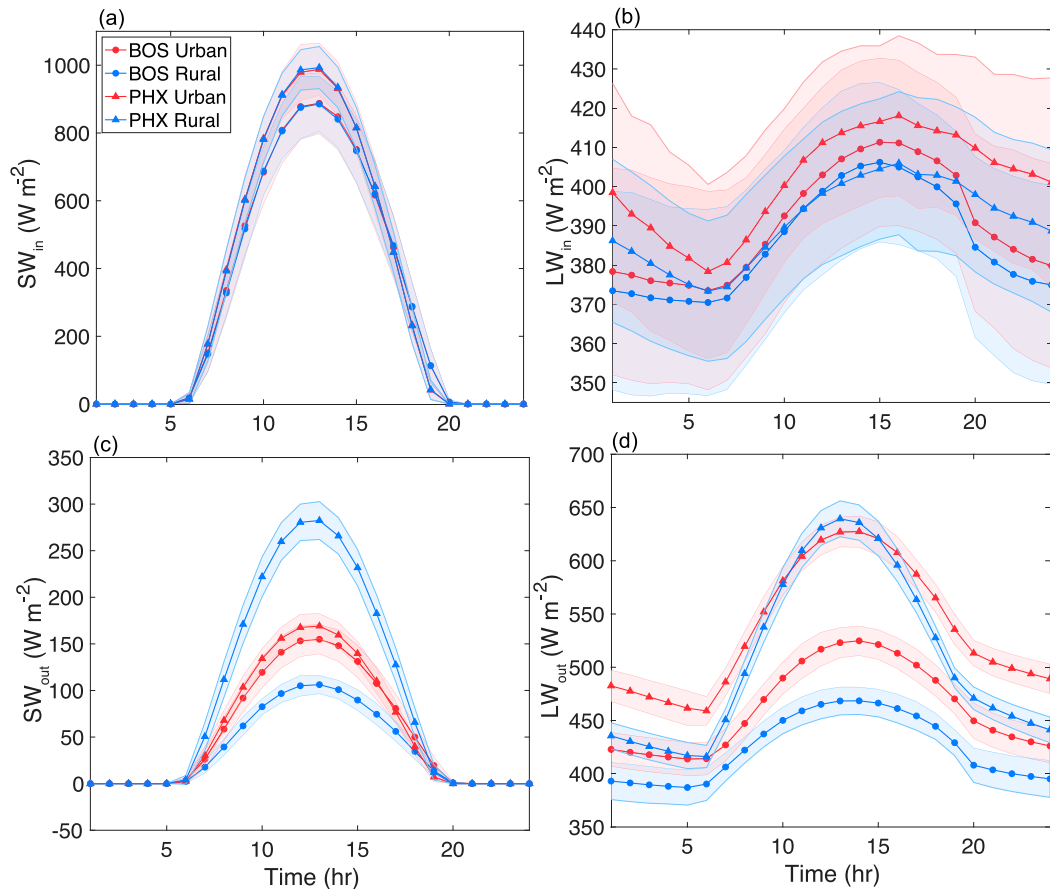


FIG. 6. As in Fig. 5, but for (a) incoming shortwave radiation SW_{in} , (b) incoming longwave radiation LW_{in} , (c) outgoing shortwave radiation SW_{out} , and (d) outgoing longwave radiation LW_{out} .

radiation. Conversely, the urban land of Phoenix has a smaller surface albedo than the rural land of Phoenix (shrubs) and thus reflects less shortwave radiation.

The urban–rural contrast in the incoming longwave radiation is positive for both cities (Fig. 6b), which is consistent with the findings from previous studies using flux tower measurements in other metropolitan regions (Li et al. 2015; Ao et al. 2019). The incoming longwave radiation is dependent on the temperature and humidity profiles in the whole atmospheric column (Brutsaert 2005) and thus it is difficult to identify exactly which factors cause such differences. In terms of urban–rural difference in outgoing longwave radiation (Fig. 6d), the results in both cities are consistent with the expectation that the outgoing longwave radiation difference should be of the same sign as the surface temperature difference (Fig. 5a; i.e., a hotter surface tends to have larger outgoing longwave radiation).

Now we examine the turbulent fluxes. During the daytime, the urban sensible heat flux is much larger than the rural one in both cities (Fig. 7a), with a significant time lag in Boston that has been also observed by other studies (Oke et al. 2017; Ramamurthy et al. 2014). To explain this daytime urban–rural difference in sensible heat flux, we first note that the urban–rural difference in T_a is very small for both cities (less than 0.1 K) (Fig. 7c). This is again because T_a in our study refers to

the potential temperature at the lowest level of the atmospheric model (~ 30 m). The dynamics of T_a are controlled by horizontal advection of heat and mixing in the boundary layer, which are complicated and simulated by the atmospheric component of the WRF Model. However, it is not surprising that the urban–rural differences of T_a are smaller than the surface and 2-m air temperature differences due to the mixing power of surface-layer turbulence. With this in mind, we further note that the urban–rural difference in sensible heat flux is strongly modulated by aerodynamic resistances (i.e., r_a and r'_a) according to Eqs. (2) and (6). During the daytime, the urban–rural difference in r_a is positive in Boston but negative in Phoenix (Figs. 8a,b). This implies that the urban land is more efficient in convecting heat from the surface to the lower atmosphere than the rural land in Phoenix, but the opposite is true in Boston. This is broadly consistent with the fact that the rural land of Phoenix is short shrubs and thus has lower surface roughness, while the rural land of Boston is tall forests and thus has higher surface roughness. Typically, larger obstacles generate more turbulence with which the heat can be transferred more efficiently from the surface to the overlying air, although we stress that convective heat transfer is fundamentally different from momentum transfer (Brutsaert 1982; Garratt 1992). Here the aerodynamic resistance refers to the resistance

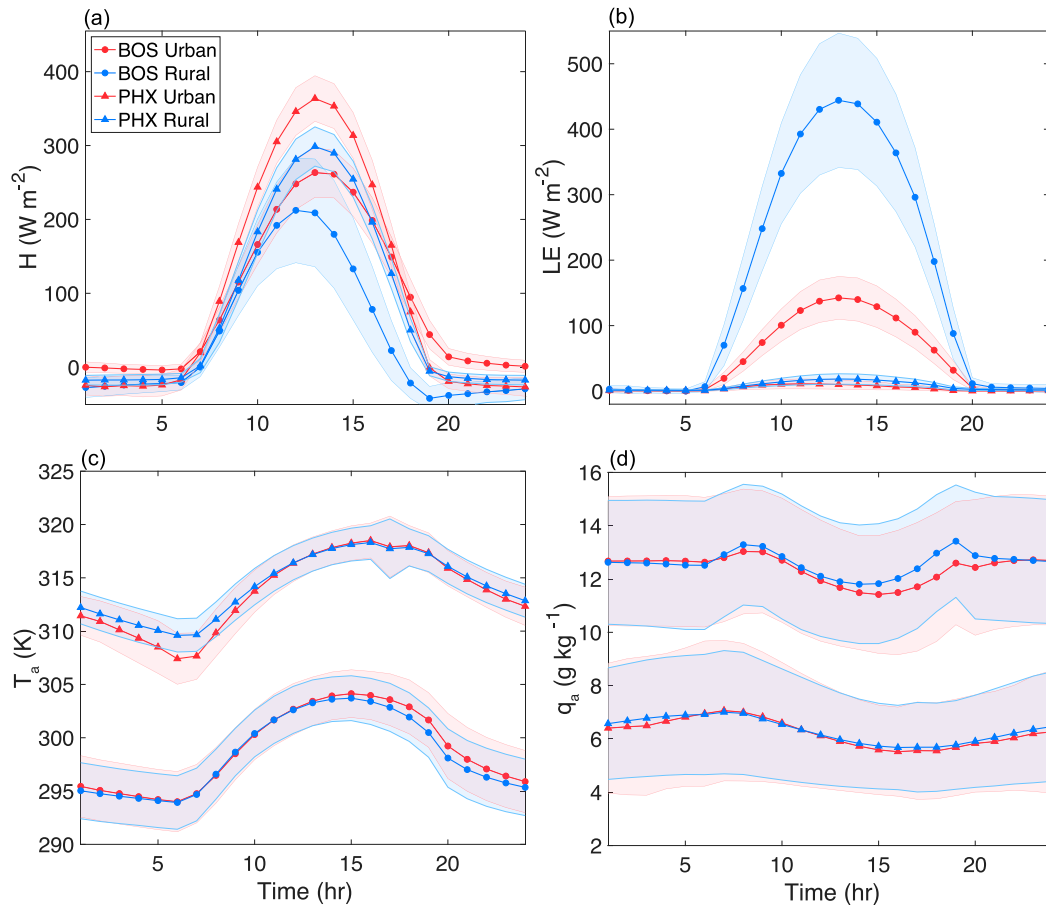


FIG. 7. As in Fig. 5, but for (a) sensible heat flux H , (b) latent heat flux LE , (c) potential temperature T_a at the lowest level of the atmospheric model, and (d) specific humidity q_a at the lowest level of the atmospheric model.

to convective heat transfer, not to momentum transfer. In comparison, the urban–rural difference in r'_a is smaller for both Boston and Phoenix (Figs. 8c,d). This highlights the important difference between r_a and r'_a and demonstrates the height dependence of aerodynamic resistance as alluded to earlier. During the nighttime, sensible heat flux becomes negative (Fig. 7a), indicating that the lower atmosphere in turn heats the surface. The magnitude of the urban sensible heat flux is smaller than the rural sensible heat flux in Boston but larger in Phoenix (Fig. 7a), which indicates that the urban land in Boston (Phoenix) has a weaker (stronger) capacity to transfer heat from the overlying air to the surface than the rural land at night. Combined with the daytime results, this reflects that the urban land is less (more) efficient than the rural land in convecting heat between the land surface and the lowest model level in Boston (Phoenix).

During the daytime, the urban latent heat flux is much lower than the rural latent heat flux in Boston, while in Phoenix both urban and rural latent heat fluxes are extremely small (Fig. 7b). In both cities, the urban–rural differences in latent heat flux are not caused by the differences in the specific humidity at the lowest level of the atmospheric model, which are very small (Fig. 7d). According to Eq. (3), the latent heat flux is strongly modulated by surface resistance in addition to aerodynamic

resistance. We use Eq. (3) to infer the surface resistance and find that the urban surface resistance is larger than the rural surface resistance in Boston during the daytime (Fig. 8e). This explains why the urban latent heat flux is much smaller than the rural counterpart in Boston during the daytime. Both urban and rural surface resistances in Phoenix inferred from Eq. (3) are exceptionally large due to the desert climate (Fig. 8f). During the nighttime, there are rather small urban–rural differences in latent heat flux for both cities as urban and rural latent heat fluxes tend to be close to zero (Fig. 7b).

Last but not the least, we examine the ground heat flux. Between the two cities, the magnitude of rural ground heat flux differs strongly: the forests in Boston have much smaller ground heat fluxes than the shrubs in Phoenix (Fig. 9). This has been observed before and is due to the difference in the canopy height: a taller canopy tends to reduce the shortwave radiation reaching the ground and thus has less ground heat flux (Garratt 1992). When the urban and rural ground heat fluxes are compared, we find that in both cities, the urban ground heat flux is on average larger than the rural ground heat flux during the daytime (Fig. 9), but it is more negative during the nighttime. The results indicate that in both cities the urban land stores more energy into the ground than the rural land during the

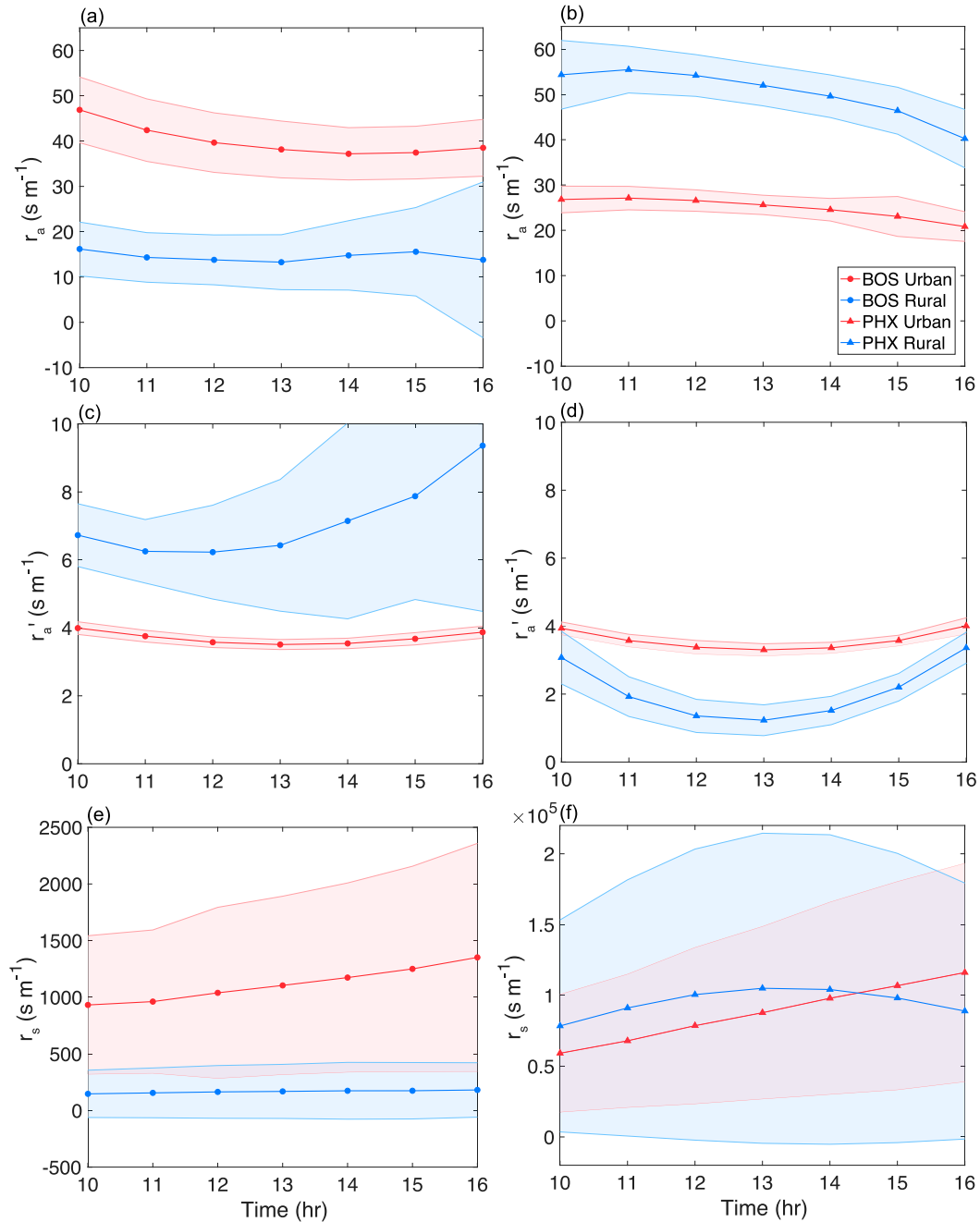


FIG. 8. The inferred resistances from WRF simulations, including (a),(b) aerodynamic resistance r_a between the surface and the lowest atmospheric model level; (c),(d) aerodynamic resistance r'_a between the 2-m level and the lowest atmospheric model level; and (e),(f) surface resistance r_s , for (left) Boston and (right) Phoenix. The shading denotes standard deviations. Time represents the local standard time. Only the daytime (1000–1600 local standard time) results are shown.

daytime. As a result, the urban surface and near-surface air are heated more at night due to the heat storage release.

c. Attribution results

While the results shown in the previous section are informative, they do not directly quantify the contributions

of different factors to the magnitude of UHIs. To do so, we apply the TRM attribution method to the WRF-simulated UHIs and UCIs in terms of surface temperature T_s [section 3c(1)] and 2-m air temperature T_2 [section 3c(2)]. The comparison between Boston and Phoenix results is presented in section 3c(3).

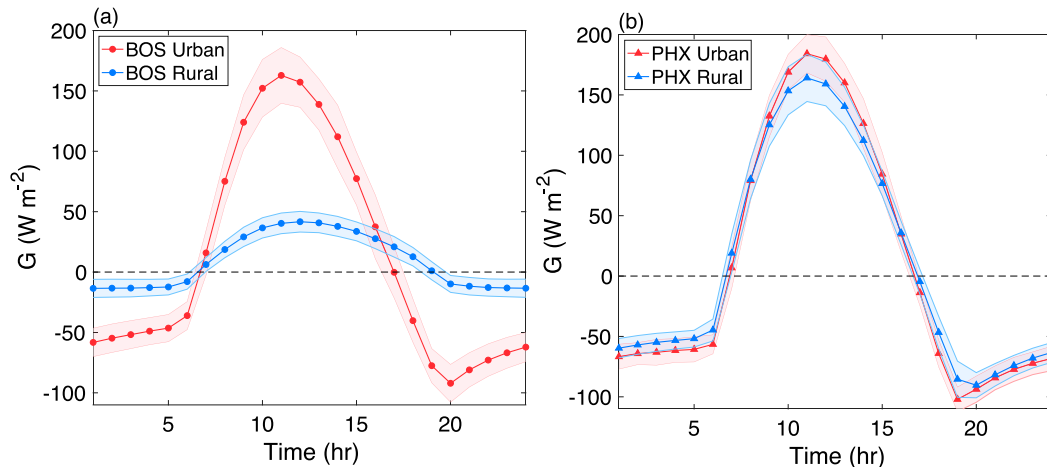


FIG. 9. Average diurnal cycles of ground heat flux G from WRF simulations in (a) Boston and (b) Phoenix. The shading denotes standard deviations. Time represents the local standard time.

The credibility of the TRM method is supported by the consistency between the TRM-modeled (Figs. 10 and 11, red bars) and the WRF-simulated (Figs. 10 and 11, orange bars) urban-rural temperature differences. Based on the TRM-modeled results, we find an SUHI ($\Delta T_s = 6.1 \text{ K}$) in Boston but a SUCI ($\Delta T_s = -3.3 \text{ K}$) in Phoenix during the daytime (Fig. 10). At night, we find an SUHI ($\Delta T_s = 3.3 \text{ K}$) in Boston and also an SUHI ($\Delta T_s = 3.7 \text{ K}$) in Phoenix. In terms of the AUHI, we find almost no daytime AUHIs in both cities (Fig. 11). At night, we find an AUHI ($\Delta T_2 = 2.4 \text{ K}$) in Boston and no AUHI in Phoenix. In the

following, we discuss the individual contributions from different factors to SUHIs and AUHIs (Figs. 10 and 11, blue bars). The individual sensitivities and urban-rural differences are presented in Tables 3–5. Note that the values reported in Tables 3–5 are the median values of the results over all HW days.

1) SUHI ATTRIBUTION RESULTS

(i) Boston

During the daytime, the urban-rural difference in the surface temperature (ΔT_s) in Boston is mainly contributed by r_s

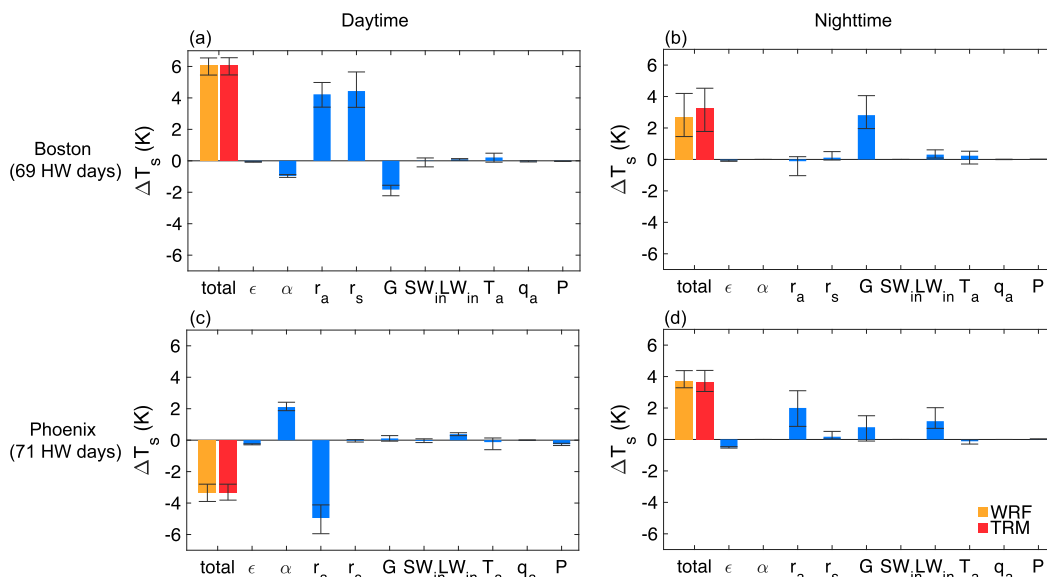


FIG. 10. Attribution of surface urban heat islands (ΔT_s ; urban minus rural surface temperature) using the TRM model during (a),(c) daytime (1000–1600) and (b),(d) nighttime (2200–0400) in (top) Boston and (bottom) Phoenix. The orange and red bars represent WRF-simulated and TRM-modeled ΔT_s , respectively. The blue bars represent contributions from different factors, including emissivity ϵ , albedo α , r_a , r_s , G , SW_{in} , LW_{in} , T_a , q_a , and pressure P . The sample size is noted in parentheses on the left. The column indicates the median of the attribution results at the daily scale. The error bars are the 80th and 20th percentiles of the results, respectively, representing the day-to-day variability of the attribution results.

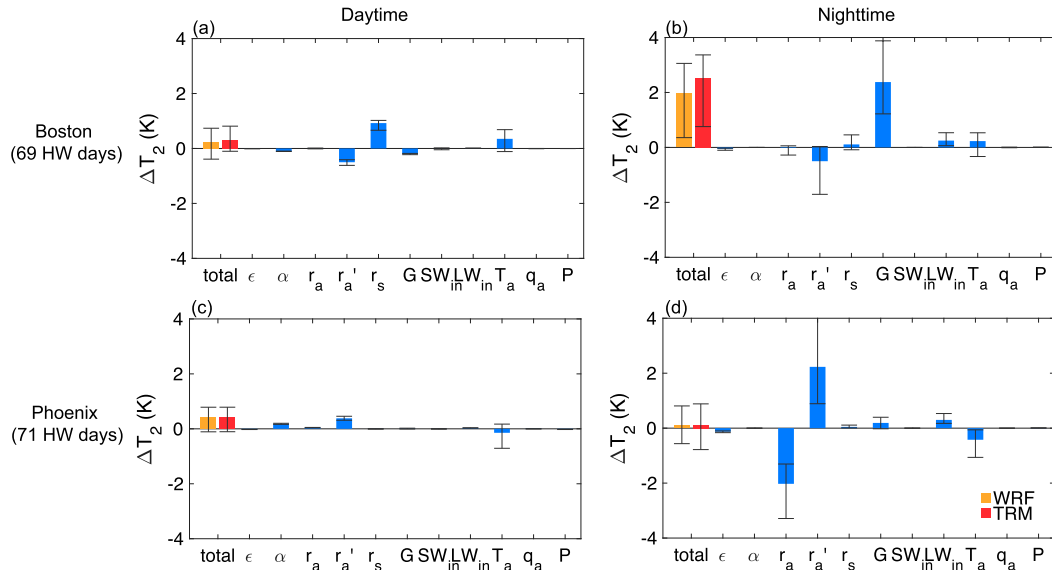


FIG. 11. As in Fig. 10, but for near-surface air urban heat islands (ΔT_2 ; urban minus rural 2-m air potential temperature) instead of ΔT_s and adding r'_a to the contributions from different factors.

(+73.3%), r_a (+69.9%), G (−30.2%), and α (−15.9%) (see Fig. 10a). Hence the hotter urban surface in Boston during the daytime, when compared to the rural surface (forests), is mainly caused by the drier nature (i.e., a larger urban r_s) and the lower heat transfer efficiency between the surface and the lower atmosphere (i.e., a larger urban r_a). The larger G and the larger α tend to lower the urban surface temperature but do not overcome the positive contributions from the resistances. Specifically, the sensitivity of T_s to r_s is positive (Table 3), implying that a drier surface tends to be hotter. Therefore, the r_s makes a large positive contribution to the ΔT_s due to the larger urban r_s than the rural r_s in Boston (Table 5). The sensitivity of T_s to r_a is also positive (Table 3), indicating that a surface with a larger r_a tends to be hotter during the daytime. This is because with a larger r_a it is more difficult to convect the heat to the atmosphere. As the urban r_a is larger than the rural r_a in Boston (Table 5), the r_a also makes a large positive contribution to the ΔT_s . The sensitivity of T_s to α is negative (Table 3), showing that a darker surface tends to be hotter. Thus, the α makes a negative contribution to the ΔT_s as the urban surface has a larger α than the rural surface in Boston (Table 5). The sensitivity of T_s to G is also negative (Table 3), which means that a larger ground heat flux going into the soil or built materials tends to cause a cooler surface during the

daytime. Therefore, the larger urban G (Table 5) results in a negative contribution to the ΔT_s .

The nighttime ΔT_s in Boston is primarily contributed by G (see Fig. 10b). That is, the hotter urban surface mostly results from the larger heat storage release at night. The sensitivity of T_s to G is negative (Table 3), which indicates that the surface becomes hotter when there is a larger release of the heat storage (i.e., a more negative G). Thus, when the urban G is smaller (i.e., more negative) than the rural G (Table 5 and Fig. 9a), the G makes a positive contribution to the ΔT_s .

(ii) Phoenix

In Phoenix, the daytime ΔT_s is mainly contributed by r_a (−159.7%) and α (+67.9%) (see Fig. 10c). Hence the cooler urban surface in Phoenix during the daytime is mainly because the urban areas have a stronger convective heat transfer efficiency compared to the rural areas. Although the urban surface is darker in Phoenix, it does not overcome the negative contribution from the aerodynamic resistance.

The nighttime ΔT_s in Phoenix is mainly contributed by r_a (+56.9%), LW_{in} (+33.0%), and G (+22.1%). Namely, the hotter urban surface is caused by its lower urban aerodynamic resistance, the larger urban incoming longwave radiation, and the stronger heat storage release. While the latter two factors

TABLE 3. Sensitivities of surface temperature to changes in various factors; DB = daytime Boston, DP = daytime Phoenix, NB = nighttime Boston, and NP = nighttime Phoenix. The value is the median of the results at the daily scale.

	$\partial T_s / \partial \epsilon$ (K)	$\partial T_s / \partial \alpha$ (K)	$\partial T_s / \partial r_a$ (K m s ^{−1})	$\partial T_s / \partial r_s$ (K m s ^{−1})	$\partial T_s / \partial G$ (K m ² W ^{−1})	$\partial T_s / \partial SW_{in}$ (K m ² W ^{−1})	$\partial T_s / \partial LW_{in}$ (K m ² W ^{−1})	$\partial T_s / \partial T_a$ (—)	$\partial T_s / \partial q_a$ (K)	$\partial T_s / \partial P$ (K Pa ^{−1})
DB	-3×10^0	-2×10^1	2×10^{-1}	7×10^{-3}	-2×10^{-2}	2×10^{-2}	2×10^{-2}	7×10^{-1}	1×10^2	-5×10^{-5}
DP	-5×10^0	-2×10^1	3×10^{-1}	5×10^{-5}	-2×10^{-2}	2×10^{-2}	2×10^{-2}	8×10^{-1}	6×10^0	-8×10^{-5}
NB	-3×10^0	0	-4×10^{-3}	6×10^{-6}	-7×10^{-2}	6×10^{-2}	7×10^{-2}	6×10^{-1}	3×10^1	1×10^{-5}
NP	-1×10^1	0	-1×10^{-3}	4×10^{-7}	-1×10^{-1}	1×10^{-1}	1×10^{-1}	2×10^{-1}	4×10^0	1×10^{-5}

TABLE 4. As in Table 3, but for 2-m air temperature.

	$\partial T_2/\partial \varepsilon$ (K)	$\partial T_2/\partial \alpha$ (K)	$\partial T_2/\partial r_a$ (K m s ⁻¹)	$\partial T_2/\partial r'_a$ (K m s ⁻¹)	$\partial T_2/\partial r_s$ (K m s ⁻¹)	$\partial T_2/\partial G$ (K m ² W ⁻¹)	$\partial T_2/\partial SW_{in}$ (K m ² W ⁻¹)	$\partial T_2/\partial LW_{in}$ (K m ² W ⁻¹)	$\partial T_2/\partial T_a$ (—)	$\partial T_2/\partial q_a$ (K)	$\partial T_2/\partial P$ (K Pa ⁻¹)
DB	-3×10^{-1}	-2×10^0	-1×10^{-4}	2×10^{-1}	1×10^{-3}	-2×10^{-3}	2×10^{-3}	2×10^{-3}	1×10^0	2×10^1	-5×10^{-6}
DP	-5×10^{-1}	-2×10^0	-2×10^{-3}	3×10^{-1}	4×10^{-6}	-2×10^{-3}	1×10^{-3}	2×10^{-3}	1×10^0	5×10^{-1}	-6×10^{-6}
NB	-2×10^0	0	2×10^{-3}	-7×10^{-3}	5×10^{-6}	-6×10^{-2}	5×10^{-2}	5×10^{-2}	6×10^{-1}	3×10^1	2×10^{-5}
NP	-3×10^0	0	1×10^{-3}	-6×10^{-3}	1×10^{-7}	-3×10^{-2}	3×10^{-2}	3×10^{-2}	8×10^{-1}	1×10^0	2×10^{-6}

are straightforward to understand, the importance of r_a requires some explanation. The sensitivity of T_s to r_a is negative at night (Table 3), which indicates that a smaller r_a leads to a higher T_s . This is because more heat can be transferred downward to warm the surface at night. Therefore, the smaller urban r_a in Phoenix (Table 5) contributes positively to the ΔT_s . Here we highlight that the sensitivity of T_s to r_a changes its sign compared to the daytime counterpart. During the daytime, a surface with a larger r_a tends to be hotter due to the reduced efficiency to transfer sensible heat to the atmosphere. However, during the nighttime a surface with a smaller r_a tends to be hotter because it becomes easier for the atmosphere to transfer heat toward the surface. This diurnal asymmetry has been well documented in studies examining the impacts of deforestation on land surface temperature (Burakowski et al. 2018; Lee et al. 2011; Liao et al. 2018b; Schultz et al. 2017).

2) AUHI ATTRIBUTION RESULTS

Close inspection of the AUHI attribution results reveals that most factors work in a similar way as in the SUHI attribution results but with a smaller magnitude (Figs. 10 and 11). This is understandable as the 2-m air temperature is effectively derived by interpolating between the surface temperature and the potential temperature at the lowest level of the atmospheric model [see Eq. (6)]. Hence most factors affecting SUHI also impact AUHI, but the magnitude of such impact is damped due to turbulent mixing between the surface and the 2-m level, which manifests as the difference between r_a and r'_a [i.e., the f in Eq. (7)]. The major differences between the AUHI and SUHI attribution results lie in the new contributions from r'_a and the different sensitivities of T_s and T_2 to r_a , which are of opposite signs as shown in Tables 3 and 4. We will focus on these differences in this section.

(i) Boston

During the daytime, the urban–rural difference in the 2-m air temperature (ΔT_2) is mainly controlled by r_s and r'_a in Boston (see Fig. 11a). The new contribution from r'_a is negative (Fig. 11a). The sensitivity of T_2 to r'_a is three orders of magnitude larger than the sensitivity of T_2 to r_a (Table 4), which indicates that the 2-m air temperature is more controlled by r'_a than r_a . Moreover, the sensitivity of T_2 to r'_a is positive, which means that the 2-m air temperature tends to be smaller when the heat at the 2-m level can be more easily transferred upward during the daytime (i.e., with a smaller r'_a). The urban r'_a is slightly lower than the rural r'_a in Boston (Table 5), resulting in a negative contribution to the ΔT_2 .

During the nighttime, the ΔT_2 is predominately contributed by G in Boston (see Fig. 11b). Nonetheless, the r'_a makes a negative contribution (Fig. 11b). The sensitivity of T_2 to r'_a is negative (Table 4), which has an opposite sign compared to the daytime counterpart because the heat is transferred upward in the day but downward at night. As the r'_a becomes larger, it is more difficult for the heat to be transferred downward to warm the near-surface air at 2 m at night, leading to a lower T_2 . Therefore, when r'_a is larger in urban areas than in rural areas at night (Table 5), the r'_a makes a negative contribution to the ΔT_2 . The magnitude of the sensitivity of T_2 to r'_a is also 3.5 times that of the sensitivity of T_2 to r_a , explaining why the contribution from r_a is much smaller than that from r'_a .

TABLE 5. As in Table 3, but for urban–rural differences in terms of various factors (Δ : urban minus rural values).

	$\Delta\varepsilon$ (–)	$\Delta\alpha$ (–)	Δr_a (s m^{-1})	$\Delta r'_a$ (s m^{-1})	Δr_s (s m^{-1})	ΔG (W m^{-2})	$\Delta \text{SW}_{\text{in}}$ (W m^{-2})	$\Delta \text{LW}_{\text{in}}$ (W m^{-2})	ΔT_a (K)	Δq_a (kg kg^{-1})	ΔP (Pa)
DB	2×10^{-2}	5×10^{-2}	2×10^1	-3×10^0	6×10^2	8×10^1	6×10^{-1}	4×10^0	4×10^{-1}	-4×10^{-4}	6×10^2
DP	5×10^{-2}	-1×10^{-1}	-2×10^1	2×10^0	-1×10^3	-5×10^0	-3×10^0	2×10^1	-1×10^{-1}	-4×10^{-5}	3×10^3
NB	2×10^{-2}	5×10^{-2}	-2×10^1	1×10^1	2×10^4	-4×10^1	0	5×10^0	5×10^{-1}	2×10^{-5}	5×10^2
NP	5×10^{-2}	-1×10^{-1}	-2×10^3	-4×10^2	4×10^5	-6×10^0	0	9×10^0	-6×10^{-1}	-2×10^{-4}	2×10^3

(ii) Phoenix

In Phoenix, the daytime ΔT_2 is more controlled by r'_a than r_a , with also some positive contribution from α (Fig. 11c). This is because the sensitivity of T_2 to r'_a is positive and two orders of magnitude larger than the sensitivity of T_2 to r_a (Table 4). This is similar to the Boston results and again indicates that a larger r'_a results in a higher T_2 because it is more difficult for heat at the 2-m level to be transferred to the atmosphere above during the daytime. Therefore, the larger urban r'_a (Table 5) leads to a positive contribution to the ΔT_2 .

During the nighttime, both r'_a and r_a make important contributions to ΔT_2 (Fig. 11d), but they play opposite roles and roughly cancel each other. The sensitivity of T_2 to r'_a is negative at night (Table 4), which indicates that a lower r'_a raises T_2 as the near-surface air can gain heat more easily from the atmosphere above. Thus, the smaller urban r'_a makes a positive contribution to the ΔT_2 . On the other hand, the r_a makes a negative contribution. The contribution from r_a changes its sign when compared to the SUHI results because the sensitivity of T_2 to r_a always has the opposite sign as the sensitivity of T_s to r_a (Tables 3 and 4). Physically this means that convection either raises the surface temperature at the expense of reducing the near-surface air temperature or raises the near-surface air temperature at the expense of reducing the surface temperature. In this case, the smaller urban r_a causes more heat to be transferred from the overlying air to the surface, which positively contributes to SUHI (Fig. 10) but negatively contributes to AUHI (Fig. 11).

3) DIFFERENCES IN THE ATTRIBUTION RESULTS BETWEEN BOSTON AND PHOENIX

Comparing the attribution results between Boston and Phoenix, we find that the major contributors work in an opposite way during the daytime due to the opposite sign of the urban–rural difference in these factors (Table 5). First, compared to the urban land, the rural land in Boston has a lower r_a but the rural land in Phoenix has a higher r_a . Thus, the urban–rural difference in the aerodynamic resistance between the surface and the lowest atmospheric model level (Δr_a) is positive in Boston but negative in Phoenix. Therefore, the r_a contribution to ΔT_s is positive in Boston, but negative in Phoenix (Figs. 10 and 11). Second, the urban–rural difference in the aerodynamic resistance between the 2-m level and the lowest atmospheric model level ($\Delta r'_a$) is negative in Boston but positive in Phoenix during the daytime (Table 5). Therefore, the contribution of r'_a to ΔT_2 is negative in Boston but positive in Phoenix (Fig. 11). Third, compared to urban areas, rural areas (forests) in Boston have lower albedo (α) while rural areas

(shrubs) in Phoenix have higher α (Table 5). Thus, the contributions of α to ΔT_s and ΔT_2 are negative in Boston, but positive in Phoenix (Figs. 10 and 11). Fourth, the urban–rural difference in surface resistance (Δr_s) is positive in Boston (Table 5), which leads to positive contributions to ΔT_s and ΔT_2 . But the urban–rural difference in surface resistance (Δr_s) has almost no effects on ΔT_s and ΔT_2 in Phoenix (Figs. 10 and 11) due to the much lower sensitivities ($\partial T_s/\partial r_s$ and $\partial T_2/\partial r_s$) (Tables 3 and 4). This indicates that the surface temperature is more sensitive to the surface moisture availability in Boston than in Phoenix, possibly due to the already very dry conditions in Phoenix.

The comparison of the nighttime results is simpler. The nighttime SUHI and AUHI in Boston are predominantly caused by the stronger urban heat storage release. For Phoenix, the contributions from r_a and r'_a are large, but the heat storage release still plays a role especially for SUHI.

4. Discussion

a. Comparison with previous studies

Our SUHI attribution results can shed important insights on the recent debate about the spatial variability of daytime SUHIs over North America. Cities with more annual rainfall, such as Boston in our case, tend to have stronger daytime SUHIs than those with less rainfall, such as Phoenix in our case, as shown by a number of previous studies (Clinton and Gong 2013; Imhoff et al. 2010; D. Li et al. 2019; Peng et al. 2012; Zhao et al. 2014). Zhao et al. (2014) found that aerodynamic resistance is the dominant factor controlling the daytime SUHI spatial variability across cities in North America at the annual mean scale. On the other hand, D. Li et al. (2019) found that it is surface resistance that more strongly controls the daytime SUHI spatial variability at the annual mean scale, although the attribution results in D. Li et al. (2019) also indicated an important role of aerodynamic resistance. Our results show that both aerodynamic resistance and surface resistance contribute significantly to the differences between Boston and Phoenix results in the daytime, which is consistent with the findings of D. Li et al. (2019) and Manoli et al. (2019) albeit at vastly different temporal scales. The importance of aerodynamic resistance for the SUHI spatial variability results from the fact that the urban–rural difference in aerodynamic resistance shows opposite signs in the two cities. Our results show that in Boston the aerodynamic resistance to convective heat transfer between the surface and the lower atmosphere is larger in urban areas than in rural areas, while the opposite is true in Phoenix. On the other hand, the importance of surface resistance for the daytime SUHI variability stems from the fact

that the urban–rural difference in surface resistance contributes strongly to the SUHI in Boston but not in Phoenix.

Our nighttime results in Boston are consistent with the traditional paradigm that the stronger release of ground heat flux in urban areas predominantly causes the nighttime SUHIs (Oke et al. 2017). However, the results in Phoenix suggest that the role of aerodynamic resistance cannot be neglected. When the land surface becomes cooler than the atmosphere at night, the sensible heat goes from the atmosphere to the surface. This transfer of heat is more efficient over surfaces with a lower r_a (the urban surface in Phoenix's case) and hence positively contributes to the nighttime SUHI. While this effect is less documented in observational studies on SUHIs, it has been demonstrated in studies on the impacts of deforestation on land surface temperature (Burakowski et al. 2018; Lee et al. 2011; Liao et al. 2018b; Schultz et al. 2017).

b. Limitations of our study

There are a few limitations of our study that are important to appreciate. First, we do not consider AF in our simulations and attributions. Within the confines of our attribution method [see Eq. (4)], the sensitivity of T_s and T_2 to AF should be identical to that to ground heat flux (G) but with an opposite sign, which is on the order of 10^{-2} – 10^{-1} K m² W⁻¹ for T_s and on the order of 10^{-3} – 10^{-2} K m² W⁻¹ for T_2 . Using the fixed diurnal profile for AF prescribed in the single-layer urban canopy model (Kusaka et al. 2001; Kusaka and Kimura 2004), the urban–rural difference in AF is estimated to be on the order of 75 W m⁻² (including both sensible and latent anthropogenic heat fluxes). Thus, the contributions of AF are estimated to be around 0.75–7.5 K for the SUHI and 0.075–0.75 K for the AUHI. We point out that the simple estimate presented here might suffer from the uncertainties associated with the magnitude of AF (Allen et al. 2011; Salamanca et al. 2014). Moreover, the simulated sensitivities of T_s and T_2 to AF depend on how exactly AF is incorporated in the energy balance computation in WRF, and they might be different from the values shown here. While these complications are left for future investigations, we note that the signs of the sensitivities of T_s and T_2 to AF and the urban–rural contrast of AF are expected to be positive. Hence AF always tends to make positive contributions to the UHIs.

Second, our analysis only focuses on HW days and thus the findings might not be extrapolated to other weather conditions. We do not investigate the responses of UHIs to HWs by comparing the results in pre-HW, HW, and post-HW days. Many studies have shown that there exist synergies between UHIs and HWs, namely, the magnitude of UHIs is larger under HWs (e.g., Ao et al. 2019; Founda et al. 2015; Founda and Santamouris 2017; Li and Bou-Zeid 2013; Li et al. 2015; Ramamurthy et al. 2017; Schatz and Kucharik 2015). However, there are also studies reporting that the magnitude of UHIs is reduced under HW conditions (e.g., Rogers et al. 2019; Scott et al. 2018). Our attribution method may shed new insights into this debate, but this is left for future research.

Third, as with most studies using models like WRF, the validation is centered on land surface temperature patterns, 2-m air temperatures at a number of weather stations, as well as the boundary layer temperature profiles at the two airports due

to data availability. Given the lack of observations, we could not directly validate the fluxes from our simulations. More thorough validation, especially on parameters and variables related to near-surface heat transfer, is recommended.

5. Conclusions

In the present study, we investigate the controlling factors of UHIs and UCIs during HWs in Boston and Phoenix using WRF simulations. During the daytime, we find an SUHI in Boston mainly caused by the higher urban r_s that reduces the latent heat flux, and the higher urban r_a that inhibits convective heat transfer from the urban surface to the atmosphere. In contrast, we find a daytime SUCI in Phoenix mainly due to the lower urban r_a that facilitates convective heat transfer. At night, we identify an SUHI and an AUHI in Boston that are due to the stronger release of urban heat storage. In comparison, the lower urban r_a in Phoenix facilitates convective heat transfer from the atmosphere to the urban surface at night, leading to an SUHI but no AUHI. Our study highlights that the magnitude of UHIs or UCIs is strongly controlled by urban–rural differences in terms of aerodynamic features, vegetation and moisture conditions, and heat storage, which show contrasting characteristics in different regions. Further investigations on the roles of anthropogenic heat flux and weather conditions and more thorough validation of the simulated results are recommended.

Acknowledgments. This material is based upon work supported by the U.S. National Science Foundation (Grant ICER-1854706) and the U.S. Army Research Office (Grant W911NF-18-1-0360). We acknowledge the high-performance computing support from Boston University Shared Computing Cluster and from Cheyenne (<https://doi.org/10.5065/D6RX99HX>) provided by NCAR's Computational and Information Systems Laboratory, sponsored by the National Science Foundation. We also thank the three reviewers whose comments led to significant improvement in the quality of our paper.

REFERENCES

- Allen, L., F. Lindberg, and C. S. B. Grimmond, 2011: Global to city scale urban anthropogenic heat flux: Model and variability. *Int. J. Climatol.*, **31**, 1990–2005, <https://doi.org/10.1002/joc.2210>.
- Anderson, G. B., and M. L. Bell, 2009: Weather-related mortality: How heat, cold, and heat waves affect mortality in the United States. *Epidemiology*, **20**, 205–213, <https://doi.org/10.1097/EDE.0b013e318190ee08>.
- , and —, 2011: Heat waves in the United States: Mortality risk during heat waves and effect modification by heat wave characteristics in 43 U.S. communities. *Environ. Health Perspect.*, **119**, 210–218, <https://doi.org/10.1289/ehp.1002313>.
- Ao, X., L. Wang, X. Zhi, W. Gu, H. Yang, and D. Li, 2019: Observed synergies between urban heat islands and heat waves and their controlling factors in Shanghai, China. *J. Appl. Meteor. Climatol.*, **58**, 1955–1972, <https://doi.org/10.1175/JAMC-D-19-0073.1>.
- Arnfield, A. J., 2003: Two decades of urban climate research: A review of turbulence, exchanges of energy and water, and the

- urban heat island. *Int. J. Climatol.*, **23**, 1–26, <https://doi.org/10.1002/joc.859>.
- Brown, S. J., J. Caesar, and C. A. T. Ferro, 2008: Global changes in extreme daily temperature since 1950. *J. Geophys. Res.*, **113**, D05115, <https://doi.org/10.1029/2006JD008091>.
- Brutsaert, W., 1982: *Evaporation into the Atmosphere: Theory, History and Applications*. Springer, 302 pp.
- , 2005: *Hydrology: An Introduction*. Cambridge University Press, 605 pp.
- Burakowski, E., A. Tawfik, A. Ouimette, L. Lepine, K. Novick, S. Ollinger, C. Zarzycki, and G. Bonan, 2018: The role of surface roughness, albedo, and Bowen ratio on ecosystem energy balance in the eastern United States. *Agric. For. Meteorol.*, **249**, 367–376, <https://doi.org/10.1016/j.agrformet.2017.11.030>.
- Campbell, S., T. A. Remenyi, C. J. White, and F. H. Johnston, 2018: Heatwave and health impact research: A global review. *Health Place*, **53**, 210–218, <https://doi.org/10.1016/j.healthplace.2018.08.017>.
- Chen, C., L. Wang, M. Ranga, and D. Li, 2020: Attribution of land-use/land-cover change induced surface temperature anomaly: How accurate is the first-order Taylor series expansion? *J. Geophys. Res. Biogeosci.*, **125**, e2020JG005787, <https://doi.org/10.1029/2020JG005787>.
- Chen, F., and Coauthors, 2011: The integrated WRF/urban modelling system: Development, evaluation, and applications to urban environmental problems. *Int. J. Climatol.*, **31**, 273–288, <https://doi.org/10.1002/joc.2158>.
- Chen, Y., and P. Zhai, 2017: Revisiting summertime hot extremes in China during 1961–2015: Overlooked compound extremes and significant changes. *Geophys. Res. Lett.*, **44**, 5096–5103, <https://doi.org/10.1002/2016GL072281>.
- Clinton, N., and P. Gong, 2013: MODIS detected surface urban heat islands and sinks: Global locations and controls. *Remote Sens. Environ.*, **134**, 294–304, <https://doi.org/10.1016/j.rse.2013.03.008>.
- Dole, R., and Coauthors, 2011: Was there a basis for anticipating the 2010 Russian heat wave? *Geophys. Res. Lett.*, **38**, L06702, <https://doi.org/10.1029/2010GL046582>.
- Donat, M. G., and Coauthors, 2013: Updated analyses of temperature and precipitation extreme indices since the beginning of the twentieth century: The HadEX2 dataset. *J. Geophys. Res. Atmos.*, **118**, 2098–2118, <https://doi.org/10.1002/jgrd.50150>.
- Dudhia, J., 1989: Numerical study of convection observed during the Winter Monsoon Experiment using a mesoscale two-dimensional model. *J. Atmos. Sci.*, **46**, 3077–3107, [https://doi.org/10.1175/1520-0469\(1989\)046<3077:NSOCOD>2.0.CO;2](https://doi.org/10.1175/1520-0469(1989)046<3077:NSOCOD>2.0.CO;2).
- Ek, M. B., K. E. Mitchell, Y. Lin, E. Rogers, P. Grunmann, V. Koren, G. Gayno, and J. D. Tarpley, 2003: Implementation of Noah land surface model advances in the National Centers for Environmental Prediction operational mesoscale Eta model. *J. Geophys. Res.*, **108**, 8851, <https://doi.org/10.1029/2002JD003296>.
- Fischer, E. M., and C. Schär, 2010: Consistent geographical patterns of changes in high-impact European heatwaves. *Nat. Geosci.*, **3**, 398–403, <https://doi.org/10.1038/ngeo866>.
- Fontana, G., A. Toreti, A. Ceglar, and G. De Sanctis, 2015: Early heat waves over Italy and their impacts on durum wheat yields. *Nat. Hazards Earth Syst. Sci.*, **15**, 1631–1637, <https://doi.org/10.5194/nhess-15-1631-2015>.
- Founda, D., and M. Santamouris, 2017: Synergies between urban heat island and heat waves in Athens (Greece), during an extremely hot summer (2012). *Sci. Rep.*, **7**, 10973, <https://doi.org/10.1038/s41598-017-11407-6>.
- , F. Pierros, M. Petrakis, and C. Zerefos, 2015: Interdecadal variations and trends of the urban heat island in Athens (Greece) and its response to heat waves. *Atmos. Res.*, **161–162**, 1–13, <https://doi.org/10.1016/j.atmosres.2015.03.016>.
- García-Herrera, R., J. Díaz, R. M. Trigo, J. Luterbacher, and E. M. Fischer, 2010: A review of the European summer heat wave of 2003. *Crit. Rev. Environ. Sci. Technol.*, **40**, 267–306, <https://doi.org/10.1080/10643380802238137>.
- Garratt, J. R., 1992: *The Atmospheric Boundary Layer*. Cambridge University Press, 316 pp.
- Georgescu, M., M. Moustauoui, A. Mahalov, and J. Dudhia, 2011: An alternative explanation of the semiarid urban area “oasis effect.” *J. Geophys. Res.*, **116**, D24113, <https://doi.org/10.1029/2011JD016720>.
- Grimm, N. B., S. H. Faeth, N. E. Golubiewski, C. L. Redman, J. Wu, X. Bai, and J. M. Briggs, 2008: Global change and the ecology of cities. *Science*, **319**, 756–760, <https://doi.org/10.1126/science.1150195>.
- Grimmond, S., 2007: Urbanization and global environmental change: Local effects of urban warming. *Geogr. J.*, **173**, 83–88, https://doi.org/10.1111/j.1475-4959.2007.232_3.x.
- Hajat, S., and Coauthors, 2006: Impact of high temperatures on mortality: Is there an added heat wave effect? *Epidemiology*, **17**, 632–638, <https://doi.org/10.1097/01.ede.0000239688.70829.63>.
- Han, J. Y., J. J. Baik, and H. Lee, 2014: Urban impacts on precipitation. *Asia-Pac. J. Atmos. Sci.*, **50**, 17–30, <https://doi.org/10.1007/s13143-014-0016-7>.
- Heaviside, C., X. M. Cai, and S. Vardoulakis, 2015: The effects of horizontal advection on the urban heat island in Birmingham and the West Midlands, United Kingdom during a heatwave. *Quart. J. Roy. Meteor. Soc.*, **141**, 1429–1441, <https://doi.org/10.1002/qj.2452>.
- Hidalgo, J., V. Masson, and L. Gimeno, 2010: Scaling the daytime urban heat island and urban-breeze circulation. *J. Appl. Meteor. Climatol.*, **49**, 889–901, <https://doi.org/10.1175/2009JAMC2195.1>.
- Homer, C., and Coauthors, 2015: Completion of the 2011 National Land Cover Database for the conterminous United States—Representing a decade of land cover change information. *Photogramm. Eng. Remote Sens.*, **81**, 345–354.
- Hong, S. Y., and J. O. J. Lim, 2006: The WRF single-moment 6-class microphysics scheme (WSM6). *J. Korean Meteor. Soc.*, **42**, 129–151.
- , Y. Noh, and J. Dudhia, 2006: A new vertical diffusion package with an explicit treatment of entrainment processes. *Mon. Wea. Rev.*, **134**, 2318–2341, <https://doi.org/10.1175/MWR3199.1>.
- Imhoff, M. L., P. Zhang, R. E. Wolfe, and L. Bounoua, 2010: Remote sensing of the urban heat island effect across biomes in the continental USA. *Remote Sens. Environ.*, **114**, 504–513, <https://doi.org/10.1016/j.rse.2009.10.008>.
- Kalverla, P. C., G. J. Duine, G. J. Steeneveld, and T. Hedde, 2016: Evaluation of the Weather Research and Forecasting Model in the Durance valley complex terrain during the KASCADE field campaign. *J. Appl. Meteor. Climatol.*, **55**, 861–882, <https://doi.org/10.1175/JAMC-D-15-0258.1>.
- Kusaka, H., and F. Kimura, 2004: Coupling a single-layer urban canopy model with a simple atmospheric model: Impact on urban heat island simulation for an idealized case. *J. Meteor. Soc. Japan*, **82**, 67–80, <https://doi.org/10.2151/jmsj.82.67>.
- , H. Kondo, Y. Kikegawa, and F. Kimura, 2001: A simple single-layer urban canopy model for atmospheric models: Comparison with multi-layer and slab models. *Bound.-Layer Meteorol.*, **101**, 329–358, <https://doi.org/10.1023/A:1019207923078>.

- Lau, N. C., and M. J. Nath, 2012: A model study of heat waves over North America: Meteorological aspects and projections for the twenty-first century. *J. Climate*, **25**, 4761–4784, <https://doi.org/10.1175/JCLI-D-11-00575.1>.
- , and —, 2014: Model simulation and projection of European heat waves in present-day and future climates. *J. Climate*, **27**, 3713–3730, <https://doi.org/10.1175/JCLI-D-13-00284.1>.
- Lee, X., and Coauthors, 2011: Observed increase in local cooling effect of deforestation at higher latitudes. *Nature*, **479**, 384–387, <https://doi.org/10.1038/nature10588>.
- Li, D., and E. Bou-Zeid, 2013: Synergistic interactions between urban heat islands and heat waves: The impact in cities is larger than the sum of its parts. *J. Appl. Meteor. Climatol.*, **52**, 2051–2064, <https://doi.org/10.1175/JAMC-D-13-02.1>.
- , and —, 2014: Quality and sensitivity of high-resolution numerical simulation of urban heat islands. *Environ. Res. Lett.*, **9**, 055001, <https://doi.org/10.1088/1748-9326/9/5/055001>.
- , and L. Wang, 2019: Sensitivity of surface temperature to land use and land cover change-induced biophysical changes: The scale issue. *Geophys. Res. Lett.*, **46**, 9678–9689, <https://doi.org/10.1029/2019GL084861>.
- , T. Sun, M. Liu, L. Yang, L. Wang, and Z. Gao, 2015: Contrasting responses of urban and rural surface energy budgets to heat waves explain synergies between urban heat islands and heat waves. *Environ. Res. Lett.*, **10**, 054009, <https://doi.org/10.1088/1748-9326/10/5/054009>.
- , W. Liao, A. J. Rigden, X. Liu, D. Wang, S. Malyshev, and E. Shevliakova, 2019: Urban heat island: Aerodynamics or imperviousness? *Sci. Adv.*, **5**, eaau4299, <https://doi.org/10.1126/sciadv.aau4299>.
- Li, H., Y. Zhou, X. Wang, X. Zhou, H. Zhang, and S. Sodoudi, 2019: Quantifying urban heat island intensity and its physical mechanism using WRF/UCM. *Sci. Total Environ.*, **650**, 3110–3119, <https://doi.org/10.1016/j.scitotenv.2018.10.025>.
- Liao, J., T. Wang, X. Wang, M. Xie, Z. Jiang, X. Huang, and J. Zhu, 2014: Impacts of different urban canopy schemes in WRF/Chem on regional climate and air quality in Yangtze River delta, China. *Atmos. Res.*, **145–146**, 226–243, <https://doi.org/10.1016/j.atmosres.2014.04.005>.
- Liao, W., and Coauthors, 2018a: Stronger contributions of urbanization to heat wave trends in wet climates. *Geophys. Res. Lett.*, **45**, 11 310–11 317, <https://doi.org/10.1029/2018GL079679>.
- , A. J. Rigden, and D. Li, 2018b: Attribution of local temperature response to deforestation. *J. Geophys. Res. Biogeosci.*, **123**, 1572–1587, <https://doi.org/10.1029/2018JG004401>.
- Luo, M., and N. C. Lau, 2017: Heat waves in southern China: Synoptic behavior, long-term change, and urbanization effects. *J. Climate*, **30**, 703–720, <https://doi.org/10.1175/JCLI-D-16-0269.1>.
- Manoli, G., and Coauthors, 2019: Magnitude of urban heat islands largely explained by climate and population. *Nature*, **573**, 55–60, <https://doi.org/10.1038/s41586-019-1512-9>.
- Meehl, G. A., and C. Tebaldi, 2004: More intense, more frequent, and longer lasting heat waves in the 21st century. *Science*, **305**, 994–997, <https://doi.org/10.1126/science.1098704>.
- Meir, T., P. M. Orton, J. Pullen, T. Holt, W. T. Thompson, and M. F. Arend, 2013: Forecasting the New York City urban heat island and sea breeze during extreme heat events. *Wea. Forecasting*, **28**, 1460–1477, <https://doi.org/10.1175/WAF-D-13-00012.1>.
- Mellor, G. L., and T. Yamada, 1974: A hierarchy of turbulence closure models for planetary boundary layers. *J. Atmos. Sci.*, **31**, 1791–1806, [https://doi.org/10.1175/1520-0469\(1974\)031<1791:AHOTCM>2.0.CO;2](https://doi.org/10.1175/1520-0469(1974)031<1791:AHOTCM>2.0.CO;2).
- Miao, S., F. Chen, M. A. LeMone, M. Tewari, Q. Li, and Y. Wang, 2009: An observational and modeling study of characteristics of urban heat island and boundary layer structures in Beijing. *J. Appl. Meteor. Climatol.*, **48**, 484–501, <https://doi.org/10.1175/2008JAMC1909.1>.
- Mlawer, E. J., S. J. Taubman, P. D. Brown, M. J. Iacono, and S. A. Clough, 1997: Radiative transfer for inhomogeneous atmospheres: RRTM, a validated correlated-*k* model for the longwave. *J. Geophys. Res.*, **102**, 16 663–16 682, <https://doi.org/10.1029/97JD00237>.
- Monteith, J., and M. Unsworth, 2007: *Principles of Environmental Physics*. Academic Press, 440 pp.
- Moon, M., D. Li, W. Liao, A. J. Rigden, and M. A. Friedl, 2020: Modification of surface energy balance during springtime: The relative importance of biophysical and meteorological changes. *Agric. For. Meteorol.*, **284**, 107905, <https://doi.org/10.1016/j.agrformet.2020.107905>.
- Mora, C., and Coauthors, 2017: Global risk of deadly heat. *Nat. Climate Change*, **7**, 501–506, <https://doi.org/10.1038/nclimate3322>.
- Oke, T. R., 1982: The energetic basis of the urban heat island. *Quart. J. Roy. Meteor. Soc.*, **108**, 1–24, <https://doi.org/10.1002/qj.49710845502>.
- , G. Mills, A. Christen, and J. A. Voogt, 2017: *Urban Climate*. Cambridge University Press, 546 pp.
- Pal, S., and Coauthors, 2012: Spatio-temporal variability of the atmospheric boundary layer depth over the Paris agglomeration: An assessment of the impact of the urban heat island intensity. *Atmos. Environ.*, **63**, 261–275, <https://doi.org/10.1016/j.atmosenv.2012.09.046>.
- Parente, J., M. G. Pereira, M. Amraoui, and E. M. Fischer, 2018: Heat waves in Portugal: Current regime, changes in future climate and impacts on extreme wildfires. *Sci. Total Environ.*, **631–632**, 534–549, <https://doi.org/10.1016/j.scitotenv.2018.03.044>.
- Patz, J. A., D. Campbell-Lendrum, T. Holloway, and J. A. Foley, 2005: Impact of regional climate change on human health. *Nature*, **438**, 310–317, <https://doi.org/10.1038/nature04188>.
- Peng, R. D., J. F. Bobb, C. Tebaldi, L. McDaniel, M. L. Bell, and F. Dominici, 2011: Toward a quantitative estimate of future heat wave mortality under global climate change. *Environ. Health Perspect.*, **119**, 701–706, <https://doi.org/10.1289/ehp.1002430>.
- Peng, S., and Coauthors, 2012: Surface urban heat island across 419 global big cities. *Environ. Sci. Technol.*, **46**, 696–703, <https://doi.org/10.1021/es2030438>.
- Perkins, S. E., 2015: A review on the scientific understanding of heatwaves—Their measurement, driving mechanisms, and changes at the global scale. *Atmos. Res.*, **164–165**, 242–267, <https://doi.org/10.1016/j.atmosres.2015.05.014>.
- Petersen, R. A., 2016: On the impact and benefits of AMDAR observations in operational forecasting—Part I: A review of the impact of automated aircraft wind and temperature reports. *Bull. Amer. Meteor. Soc.*, **97**, 585–602, <https://doi.org/10.1175/BAMS-D-14-00055.1>.
- Petkova, E. P., H. Morita, and P. L. Kinney, 2014: Health impacts of heat in a changing climate: How can emerging science inform urban adaptation planning? *Curr. Epidemiol. Rep.*, **1**, 67–74, <https://doi.org/10.1007/s40471-014-0009-1>.
- Pleim, J. E., 2007: A combined local and nonlocal closure model for the atmospheric boundary layer. Part I: Model description and testing. *J. Appl. Meteor. Climatol.*, **46**, 1383–1395, <https://doi.org/10.1175/JAM2539.1>.
- Ramamurthy, P., and E. Bou-Zeid, 2016: Heatwaves and urban heat islands: A comparative analysis of multiple cities. *J. Geophys. Res. Atmos.*, **122**, 168–178, <https://doi.org/10.1002/2016JD025357>.

- , —, J. A. Smith, Z. Wang, M. L. Baeck, N. Z. Saliendra, J. L. Hom, and C. Welty, 2014: Influence of subfacet heterogeneity and material properties on the urban surface energy budget. *J. Appl. Meteor. Climatol.*, **53**, 2114–2129, <https://doi.org/10.1175/JAMC-D-13-0286.1>.
- , D. Li, and E. Bou-Zeid, 2017: High-resolution simulation of heatwave events in New York City. *Theor. Appl. Climatol.*, **128**, 89–102, <https://doi.org/10.1007/s00704-015-1703-8>.
- Rigden, A. J., and D. Li, 2017: Attribution of surface temperature anomalies induced by land use and land cover changes. *Geophys. Res. Lett.*, **44**, 6814–6822, <https://doi.org/10.1002/2017GL073811>.
- Robinson, P. J., 2001: On the definition of a heat wave. *J. Appl. Meteor.*, **40**, 762–775, [https://doi.org/10.1175/1520-0450\(2001\)040<0762:OTDOAH>2.0.CO;2](https://doi.org/10.1175/1520-0450(2001)040<0762:OTDOAH>2.0.CO;2).
- Rogers, C. D. W., A. J. E. Gallant, and N. J. Tapper, 2019: Is the urban heat island exacerbated during heatwaves in southern Australian cities? *Theor. Appl. Climatol.*, **137**, 441–457, <https://doi.org/10.1007/s00704-018-2599-x>.
- Rübelke, D. T. G., and S. Vögele, 2011: Impacts of climate change on European critical infrastructures: The case of the power sector. *Environ. Sci. Policy*, **14**, 53–63, <https://doi.org/10.1016/j.envsci.2010.10.007>.
- Salamanca, F., M. Georgescu, A. Mahalov, M. Moustauoui, and M. Wang, 2014: Anthropogenic heating of the urban environment due to air conditioning. *J. Geophys. Res. Atmos.*, **119**, 5949–5965, <https://doi.org/10.1002/2013JD021225>.
- , Y. Zhang, M. Barlage, F. Chen, A. Mahalov, and S. Miao, 2018: Evaluation of the WRF-urban modeling system coupled to Noah and Noah-MP land surface models over a semiarid urban environment. *J. Geophys. Res. Atmos.*, **123**, 2387–2408, <https://doi.org/10.1002/2018JD028377>.
- Schär, C., P. L. Vidale, D. Lüthi, C. Frei, C. Häberli, M. A. Liniger, and C. Appenzeller, 2004: The role of increasing temperature variability in European summer heatwaves. *Nature*, **427**, 332–336, <https://doi.org/10.1038/nature02300>.
- Schatz, J., and C. J. Kucharik, 2015: Urban climate effects on extreme temperatures in Madison, Wisconsin, USA. *Environ. Res. Lett.*, **10**, 094024, <https://doi.org/10.1088/1748-9326/10/9/094024>.
- Schultz, N. M., P. J. Lawrence, and X. Lee, 2017: Global satellite data highlights the diurnal asymmetry of the surface temperature response to deforestation. *J. Geophys. Res. Biogeosci.*, **122**, 903–917, <https://doi.org/10.1002/2016JG003653>.
- Scott, A. A., D. W. Waugh, and B. F. Zaitchik, 2018: Reduced urban heat island intensity under warmer conditions. *Environ. Res. Lett.*, **13**, 064003, <https://doi.org/10.1088/1748-9326/aabd6c>.
- Sillmann, J., V. V. Kharin, F. W. Zwiers, X. Zhang, and D. Bronaugh, 2013: Climate extremes indices in the CMIP5 multimodel ensemble: Part II. Future climate projections. *J. Geophys. Res. Atmos.*, **118**, 2473–2493, <https://doi.org/10.1002/jgrd.50188>.
- Stewart, I. D., 2011: A systematic review and scientific critique of methodology in modern urban heat island literature. *Int. J. Climatol.*, **31**, 200–217, <https://doi.org/10.1002/joc.2141>.
- Taha, H., 1997: Urban climates and heat islands: Albedo, evapotranspiration, and anthropogenic heat. *Energy Build.*, **25**, 99–103, [https://doi.org/10.1016/S0378-7788\(96\)00999-1](https://doi.org/10.1016/S0378-7788(96)00999-1).
- Tan, J., and Coauthors, 2010: The urban heat island and its impact on heat waves and human health in Shanghai. *Int. J. Biometeor.*, **54**, 75–84, <https://doi.org/10.1007/s00484-009-0256-x>.
- Tebaldi, C., K. Hayhoe, J. M. Arblaster, and G. A. Meehl, 2006: Going to the extremes: An intercomparison of model-simulated historical and future changes in extreme events. *Climatic Change*, **79**, 185–211, <https://doi.org/10.1007/s10584-006-9051-4>.
- Tewari, M., J. Yang, H. Kusaka, F. Salamanca, C. Watson, and L. Treinish, 2019: Interaction of urban heat islands and heat waves under current and future climate conditions and their mitigation using green and cool roofs in New York City and Phoenix, Arizona. *Environ. Res. Lett.*, **14**, 034002, <https://doi.org/10.1088/1748-9326/aaf431>.
- Theeuwes, N. E., G. J. Steeneveld, R. J. Ronda, M. W. Rotach, and A. A. M. Holtslag, 2015: Cool city mornings by urban heat. *Environ. Res. Lett.*, **10**, 114022, <https://doi.org/10.1088/1748-9326/10/11/114022>.
- United Nations, 2019: *World Urbanization Prospects: The 2018 Revision*. United Nations, 103 pp.
- Wang, L., and D. Li, 2019: Modulation of the urban boundary-layer heat budget by a heatwave. *Quart. J. Roy. Meteor. Soc.*, **145**, 1814–1831, <https://doi.org/10.1002/qj.3526>.
- , —, N. Zhang, J. Sun, and W. Guo, 2020: Surface urban heat and cool islands and their drivers: An observational study in Nanjing, China. *J. Appl. Meteor. Climatol.*, **59**, 1987–2000, <https://doi.org/10.1175/JAMC-D-20-0089.1>.
- Wang, P., D. Li, W. Liao, A. Rigden, and W. Wang, 2019: Contrasting evaporative responses of ecosystems to heatwaves traced to the opposing roles of vapor pressure deficit and surface resistance. *Water Resour. Res.*, **55**, 4550–4563, <https://doi.org/10.1029/2019WR024771>.
- Wreford, A., and W. N. Adger, 2010: Adaptation in agriculture: Historic effects of heat waves and droughts on UK agriculture. *Int. J. Agric. Sustainability*, **8**, 278–289, <https://doi.org/10.3763/ijas.2010.0482>.
- Xia, J., K. Tu, Z. Yan, and Y. Qi, 2016: The super-heat wave in eastern China during July–August 2013: A perspective of climate change. *Int. J. Climatol.*, **36**, 1291–1298, <https://doi.org/10.1002/joc.4424>.
- Xia, Y., and Coauthors, 2018: Assessment of the economic impacts of heat waves: A case study of Nanjing, China. *J. Clean. Prod.*, **171**, 811–819, <https://doi.org/10.1016/j.jclepro.2017.10.069>.
- Yang, X., L. R. Leung, N. Zhao, C. Zhao, Y. Qian, K. Hu, X. Liu, and B. Chen, 2017: Contribution of urbanization to the increase of extreme heat events in an urban agglomeration in east China. *Geophys. Res. Lett.*, **44**, 6940–6950, <https://doi.org/10.1002/2017GL074084>.
- Zampieri, M., A. Ceglar, F. Dentener, and A. Toreti, 2017: Wheat yield loss attributable to heat waves, drought and water excess at the global, national and subnational scales. *Environ. Res. Lett.*, **12**, 064008, <https://doi.org/10.1088/1748-9326/aa723b>.
- Zhang, N., X. Wang, and Z. Peng, 2014: Large-eddy simulation of mesoscale circulations forced by inhomogeneous urban heat island. *Bound.-Layer Meteor.*, **151**, 179–194, <https://doi.org/10.1007/s10546-013-9879-x>.
- Zhang, Y., D. Li, Z. Lin, J. A. Santanello, and Z. Gao, 2019: Development and evaluation of a long-term data record of planetary boundary layer profiles from aircraft meteorological reports. *J. Geophys. Res. Atmos.*, **124**, 2008–2030, <https://doi.org/10.1029/2018JD029529>.
- , L. Wang, J. A. Santanello, Z. Pan, Z. Gao, and D. Li, 2020: Aircraft observed diurnal variations of the planetary boundary layer under heat waves. *Atmos. Res.*, **235**, 104801, <https://doi.org/10.1016/j.atmosres.2019.104801>.
- Zhao, L., X. Lee, R. B. Smith, and K. Oleson, 2014: Strong contributions of local background climate to urban heat islands. *Nature*, **511**, 216–219, <https://doi.org/10.1038/nature13462>.